



UNIVERSITY OF SALERNO

DEPARTMENT OF INDUSTRIAL ENGINEERING

*Ph. D. Thesis in
Mechanical Engineering*

XIII CYCLE N.S. (2011-2014)

***“Theoretical and experimental analysis of
microwave heating processes”***

Laura Giordano

Supervisor

***Ch.mo Prof. Ing.
Gennaro Cuccurullo***

Coordinator

***Ch.mo. Prof. Ing.
Vincenzo Sergi***

*Alla mia famiglia
e a tutte le persone che mi vogliono bene*

Table of contents

INDEX OF FIGURES	VII
INDEX OF TABLES	IX
INTRODUCTION.....	1
CHAPTER 1.....	7
Theoretical principles of microwave heating	7
1.1 Electromagnetic waves.....	7
1.2 Electromagnetic field's equations in sinusoidal regime.....	9
1.3 Plane waves	10
1.4 Heat generation	13
1.5 Interaction between microwaves and materials.....	14
CHAPTER 2.....	17
Batch tests: apples microwave drying.....	17
2.1 Experimental set-up.....	17
2.2 Experimental procedure	19
2.3 Experimental results.....	20
2.3.1 Temperature control during MW heating.....	20
2.3.2 Drying curves	21
2.4 The analytical model	23
2.5 Data reduction	26
2.6 Results and discussion.....	28
CHAPTER 3.....	29
Batch tests on water and oil.....	29
3.1. The finite element method.....	29
3.2. Comsol vs Ansys HFSS: the software validation.....	30
3.3. Batch tests: the problem at hand	32
3.3.1 Basic equations.....	33
3.3.2 Experimental set-up.....	35
3.3.3 Preliminary experimental tests	35
3.3.4 Results and discussion.....	37
CHAPTER 4.....	41
Continuous flow microwave heating of liquids with constant properties	41
4.1 MW system description.....	41
4.2 Basic equations: the EM problem	42

4.3 Basic equations: the heat transfer problem	43
4.4 Numerical model.....	44
4.4.1 Geometry building	45
4.4.2 Mesh generation	45
4.5 Uniform heat generation solution: the analytical model	47
4.5.1 The Graetz problem.....	51
4.5.2 The heat dissipation problem	51
4.6 Results and discussion	51
4.6.1 Electromagnetic power generation and cross-section spatial power density profiles	51
4.6.2 Comparison between analytical and numerical temperature data	52
CHAPTER 5	57
Continuous flow microwave heating of liquids with temperature dependent dielectric properties: the hybrid solution	57
5.1 Hybrid Numerical-Analytical model definition	57
5.2 3D Complete FEM Model Description	58
5.3 The hybrid solution	60
5.3.1 The heat generation definition	60
5.3.2 The 2D analytical model	61
5.4 Results: bulk temperature analysis.....	65
CHAPTER 6	69
Quantitative IR Thermography for continuous flow microwave heating	69
6.1 Theory of thermography.....	69
6.1.1 The infrared radiations	69
6.1.2 Blackbody radiation	69
6.1.3 Non-blackbody emitters	71
6.1.4 The fundamental equation of infrared thermography	73
6.2 Experimental set-up.....	75
6.3 Temperature readout procedure.....	76
6.4 Image processing	81
6.5 Results and discussion	81
CONCLUSIONS.....	85
References	87

INDEX OF FIGURES

Figure 1.1 Electromagnetic spectrum.....	7
Figure 1.2 Electromagnetic wave propagation.....	7
Figure 1.3 Dielectric permittivity of water.....	16
Figure 2.1 Microwave pilot plant heating system	18
Figure 2.2 Real-time IR thermography for apple slices	19
Figure 2.3 Temperature fluctuations for the selected temperature levels	19
Figure 2.4 Drying curves of apple slices by hot air (dashed line) and microwave (continuous line) heating at 55, 65 and 75 °C.	22
Figure 2.5 Drying rate curves.....	22
Figure 2.6 Sample geometry	25
Figure 2.7 Analytical prediction (continuous lines) vs experimental trend (falling rate period).....	27
Figure 3.1 Scheme of the single mode cavity	31
Figure 3.2 Modulus of the “z-component” of the electric field	31
Figure 3.3 Modulus of the “x-component” of the electric field	31
Figure 3.4 Bi-dimensional map of the electric field norm	32
Figure 3.5 Scheme of the experimental setup	33
Figure 3.6 Experimental set-up	33
Figure 3.7 The thermoformed tray	35
Figure 3.8 Agar vs water θ – profiles along the tray minor axis.....	36
Figure 3.9 Point P temperature evolution.....	36
Figure 4.1 Sketch of the available experimental set-up	42
Figure 4.2 Temperature variations of water along the axis of the pipe....	46
Figure 4.3 RMSE calculated with respect to the reference solution characterized by the maximum sampling density	46
Figure 4.4 Contour plots and longitudinal distributions of specific heat generation U_{gen} along three longitudinal axes corresponding to the points, O (tube centre), A, B.	52
Figure 4.5 Cross sections, equally spaced along the X-axis, of temperature spatial distribution	53
Figure 4.6 Bulk temperature profiles	54

Figure 4.7 Temperature radial profiles.....	55
Figure 5.1 Flowchart of the assumed procedure	57
Figure 5.2 Dielectric constant, ε'	60
Figure 5.3 Relative dielectric loss, ε''	60
Figure 5.4 Heat generation along the X axis for $U_{av} = 0.08$ m/s.....	61
Figure 5.5 Interpolating function (green line) of the EH heat generation distribution (discrete points) for $U_{av} = 0.08$ m/s	63
Figure 5.6 Bulk temperature evolution for $U_{av} = 0.008$ m/s	66
Figure 5.7 Bulk temperature evolution for $U_{av} = 0.02$ m/s	66
Figure 5.8 Bulk temperature evolution for $U_{av} = 0.04$ m/s.....	66
Figure 5.9 Bulk temperature evolution for $U_{av} = 0.08$ m/s.....	66
Figure 5.10 Spatial evolution of the error on the bulk temperature prediction.....	67
Figure 5.11 Root mean square error with respect to the CN solution.....	68
Figure 6.1 Planck's curves plotted on semi-log scales	71
Figure 6.2 Schematic representation of the general thermographic measurement situation.....	73
Figure 6.3 Sketch and picture of the available MW pilot plant	76
Figure 6.4 Net apparent applicator pipe temperatures	79
Figure 6.5 Effective transmissivity for the selected temperature levels ..	80
Figure 6.6 Measured and interpolated relative shape-function f_1	80
Figure 6.7 Temperature level function f_2 obtained with a linear regression	80
Figure 6.8 The reconstructed and measured true temperature profiles @ $T_{inlet} = 55^\circ\text{C}$	80
Figure 6.9 Theoretical and experimental bulk temperatures for inlet temperatures $T_{inlet} = 40, 45$ and 50°C , and two flow rates $m = 3.2$ and 5.4 g/s.	83

INDEX OF TABLES

Table 2.1 Set temperatures, averages, temperature oscillations and standard deviations (SD) during first and second half of drying time by microwave of apple slices.	21
Table 2.2 Data reduction results.....	28
Table 3.1 Oil and water properties	37
Table 3.2 H-configuration	38
Table 3.3 V-configuration	39
Table 4.1 Dimensionless partial problems: uniform heat generation solution.....	50
Table 5.1 Dimensionless partial problems: BH and EH hybrid solutions	64
Table 5.2 Computational time for CN and BH solutions.....	68
Table 6.1 RMSE of bulk temperatures for different mass flow rates and temperature levels	82

INTRODUCTION

Thermal processing is the major processing technology in the food industry and its purpose is to extend the shelf life of food products without compromising food safety. Apart from the positive effect of food treatments, such as the inactivation of pathogens, there are also some limitations by way of partial destruction of quality attributes of products, especially heat-labile nutrients, and sensory attributes.

The technological revolution, nutritional awareness, and continuous demand of the new generation have necessitated search for new or improved food processing technologies. Presently, several new food processing technologies, including microwave heating, are investigated to improve, replace, or complement conventional processing technology.

Microwave has been successfully used to heat, dry, and sterilize many food products. Compared with conventional methods, microwave processing offers the following advantages: 1) microwave penetrates inside the food materials and, therefore, cooking takes place throughout the whole volume of food internally and rapidly, which significantly reduces the processing time; 2) since heat transfer is fast, nutrients and vitamins contents, as well as flavor, sensory characteristics, and color of food are well preserved; 3) ultrafast pasteurization or sterilization of pumpable fluids minimizes nutrient, color, and flavor losses; 4) minimum fouling depositions, because of the elimination of the hot heat transfer surfaces, since the piping used is microwave transparent and remains relatively cooler than the product; 5) energy saving because of the absence of a medium between the sample and the MW; in addition, if the system is well projected, high efficiency can be reached (some authors showed the reduction of the energy costs during drying processes using microwaves, with a further improvement using air dryer and microwaves in sequence [1]; moreover, consider the possibility to use alternative energy sources, eg. photovoltaic); 6) perfect geometry for clean-in-place system; 7) low cost in system maintenance; 8) space saving, if the system is compared with the traditional ones, based on boilers and surface heat exchangers [2].

On the other hand, there are some problems which prevent the diffusion of this technique; among them: 1) uneven temperature patterns of the food processed, due to the uneven temperature field inside the microwave

cavity; 2) temperature readout and control problems, because traditional probes fail: in particular, the thermocouples disturb the measurement and are damaged by the electric field, while fiberoptic probes allow to know the temperature only in few points; 3) difficulties in predicting the temperature field, because of coupling of three physical phenomena, that is, electromagnetic wave propagations, heat transfer and, in most of cases, fluid motion. Consider that sizing, during the design phase, and the control, during the operating phase, could be based on theoretical predictions, avoiding the so called “trial and error” approach.

To address the critical points mentioned above, during the thesis work, theoretical models were developed and experimental tests were performed, with reference to “batch” and “continuous flow” processes. Batch processes and related models are described in the former part of this thesis and encompass both apple drying and in package-processes of water and oil. The second part deals with continuous processes which are more interesting, having in mind industrial applications.

Drying processes

Drying is a thermal process, because the saturation pressure increases with temperature; as a consequence, the drying rate is related to the temperature level. This technique is widely used for food preservation, but long drying times and high temperatures are required by using sunlight or conventional hot air drying. Conventional drying turns out to be a low efficient process because of the foods low thermal conductivity and high internal resistance to moisture transfer [3-34]. Thus an increasing demand for faster procedures is arising in the food industry. In this connection, microwave (MW) driven drying processes have been studied extensively in the last decade since it is well known that they provide an efficient mean for moisture removal. In facts, it has been demonstrated that, for a large variety of foods, microwave heating considerably lowers drying times without damaging flavour, colour, nutrients of the fruit [4-11; 19;22]. Improved drying rates can be explained considering that the interior of the sample is quickly heated by internal heat generation due to MW exposition and, as a consequence, the generated vapour is forced towards the surface where it is easily removed by the air flow. Furthermore, fast vapour expulsion creates a porous structure which facilitates the transport of vapour being responsible of reduced shrinkage [12-14;20].

As a matter of facts, typically, drying processes are carried-on fixing power rather than temperature levels: this occurrence can lead to product overheating, with charring and unacceptable final quality [17;20;39-41; 46]. Thus, it is clear that temperature must be controlled [40-44] but such procedure is seldom reported in the literature [45-46], probably for the reasons outlined before.

The problems underlined above about the uneven temperature patterns and the difficulties in measuring and controlling the food temperature will be addressed by showing a new microwave drying system which allows to control the product temperature acting on the magnetron duty cycle. In particular, the temperature was controlled looking inside the MW chamber by an IR equipment, thus obtaining thermal maps with high resolution.

Drying kinetics will be analysed through the determination of the effective mass diffusivity by applying a 2D unsteady analytical model.

In-package processing of liquids

The second batch application addressed in this thesis, the in-package processing, has recently determined a growing interest in using new packaging materials-dielectric and/or magnetic-in a wide variety of applications for controlling the microwave heating of food. Packaging materials need to be microwave transparent and have a high melting point, with shapes adapted for microwave heating [47].

Wishing to perform in-package pasteurization or sterilization, there is to face the uneven temperature distribution, which determines both the magnitude of time-temperature history and the location of the cold points as functions of the composition (ionic content, moisture, density, and specific heat), shape, and size of the food [48-52;58;72], for a given equipment. In fact, unlike conventional heating, the design of the equipment can more dramatically influence the critical process parameter: the location and temperature of the coldest point. Many variables such as dielectric properties, size, geometry and arrangement of food materials affect the heating uniformity, the latter being a critical matter. It then follows that the potential application of these techniques requires an accurate study of the thermal patterns of the food. The uneven temperature field in the samples can be improved by acting both on the illuminating system and on target food. In particular, thermal response for water and oil samples, placed in a special thermoformed tray, with

different size and orientation will be studied. The first aim will be to show that temperature predictions, obtained by a commercial numerical software based on Finite Element Method (FEM), can recover experimental results. Then, uniformity in temperature distribution will be investigated both through the numerical FEM runs and the corresponding experimental tests in a pilot plant.

Continuous flow microwave heating of liquids

The second part of the work deals with the continuous flow microwave heating processes, above mentioned; this systems, respect with the batch ones, are featured by increased productivity, easier clean up, and automation. Several laboratory-based continuous-flow microwave heating systems have been used for fluid foods with different configurations [53-57]. Nowadays, the numerical approach allows a quite satisfying description of the coupled thermal-EM problems as well as an accurate identification of the effects which the operating parameters have on the process at hand [54;65-68;71-72;75-76], provided that spatial discretization is performed with care as grid dispersion may arise [74]. Starting from the pioneering work of Yee [77] in which Maxwell's equations were solved with a primitive 2D version of the Finite Difference Time Domain (FDTD) technique, remarkable contributions have been given so far. Zhang et al. [68] proposed a 3D FDTD model to describe electromagnetic field patterns, power temperature and velocity distributions in a confined liquid inside a microwave cavity. Chatterjee et al. [78] numerically analyzed the effects on the temperature distribution of a liquid in terms of the rotating container, natural convection, power sources and shape of the container. Zhu et al. [79] developed a more sophisticated procedure to solve cases with temperature-dependent dielectric permittivity and non-Newtonian liquids carrying food subjected to MW heating. Actually, FDTDs [77] and Finite Element Methods (FEMs) [62] are no doubt among the most employed for simulating MW heating problems [80].

Numerical modeling may be subject to long execution times, depending on how complex is the system being simulated as well as on the spatial and temporal discretization.

In the above connection, an evolution of numerical and analytical solutions will be presented, until the hybrid numerical-analytical technique for simulating microwave (MW) heating of laminar flow in

circular ducts. Finally, a first attempt is made for a quantitative infrared thermography temperature readout to describe in real time temperature field inside an illuminated MW cavity and compare the shape of the bulk temperature theoretical curves. Given the fact that temperature measurements are usually taken onto few points by means of fiberoptic probes, the proposed procedure is intended to promote higher resolutions than standard's. Such an approach is needed, as strongly uneven spatial distribution of the temperature field, produced by MW application, is expected. Only few authors used infrared thermography in microwave applications. Mamouni and co-workers [81-82] proposed the correlation microwave thermography technique (CMWT) for the accurate description of thermal distribution on material's surfaces. In [83] kidney-bladder system pathologies are assessed by correlating MW radiometry with temperature measurements taken by fiberoptic probes. Gerbo et al. [84] used an infrared camera to provide information about the spatial temperature distribution of water in continuous flow subjected to MW heating.

CHAPTER 1

Theoretical principles of microwave heating

1.1 Electromagnetic waves

Microwaves are electromagnetic (EM) waves at frequencies between 300 and 300000 MHz, with corresponding wavelengths of 1 to 0.001 m, respectively.

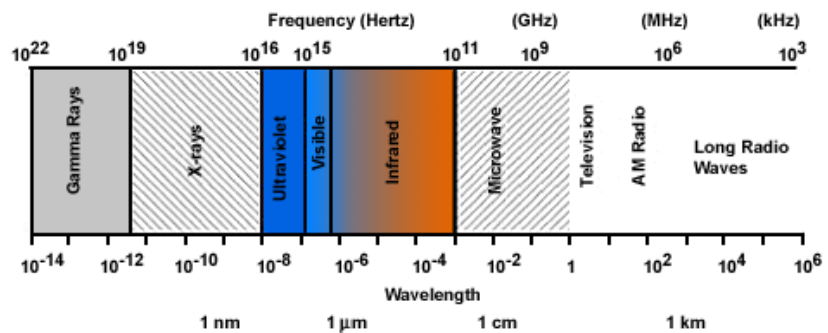


Figure 1.1 Electromagnetic spectrum

EM waves travelling in space without obstruction approximate the behaviour of plane waves; in particular, they have an electric (E) field component and a magnetic (H) field component that oscillate in phase and in directions perpendicular to each other. Both E and H components are in transverse planes (perpendicular) to the travelling direction of the EM wave, so called transverse EM (TEM) waves.

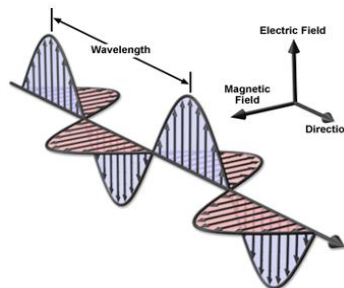


Figure 1.2 Electromagnetic wave propagation

In mathematical terms, an EM wave propagates in the direction of the cross-product of two vectors $\mathbf{E} \times \mathbf{H}$. That is, assuming that the direction of the propagation of EM waves is in the z direction as illustrated in Figure 1.2, the x - z plane contains the electric component \mathbf{E} with the electric field components directed towards the x -axis, while the y - z plane contains the magnetic component \mathbf{H} with magnetic field components directed towards the y -axis. The amplitude of an EM wave determines the maximum intensity of its field quantities.

The wavelength (λ) of an EM wave is the distance between two peaks of either electric or magnetic field. The number of cycles per second is called temporal frequency (f), whose unit is expressed in hertz (Hz). The time required for a wave to complete a cycle is referred as period (T , in second), and $T = 1/f$. Wavelength and temporal frequency are related by the equation: $\lambda = c/f$, where c is the speed of propagation and is equal to the speed of light in the free space.

The EM waves propagation is governed by Maxwell equations:

$$\nabla \times \mathbf{E} = -\frac{\partial \mathbf{B}}{\partial t} \quad (1)$$

$$\nabla \times \mathbf{H} = \frac{\partial \mathbf{D}}{\partial t} + \mathbf{J} \quad (2)$$

$$\nabla \cdot \mathbf{D} = \rho \quad (3)$$

$$\nabla \cdot \mathbf{B} = 0 \quad (4)$$

\mathbf{D} is the electric induction vector; \mathbf{B} is the magnetic induction vector; \mathbf{J} and ρ the electric current density and the density of electric charge, respectively. In particular, they are related by the continuity equation:

$$\nabla \cdot \mathbf{J} = -\frac{\partial \rho}{\partial t} \quad (5)$$

The relations between the induction vectors (\mathbf{D} and \mathbf{B}) and the electric and magnetic field vectors (\mathbf{E} and \mathbf{H}), and the relation between \mathbf{J} and \mathbf{E} , depend on the medium properties. A very simple case is the one represented by omogeneous, stationary and isotropic media; when these conditions are satisfied, the electric/magnetic vectors are parallel to the electric/magnetic fields and proportional to them by the dielectric permittivity ϵ and the dielectric permeability μ . The constitutive relations are the followings:

$$\mathbf{D} = \varepsilon \cdot \mathbf{E} = \varepsilon_0 \cdot \varepsilon_r \cdot \mathbf{E} \quad (6)$$

$$\mathbf{B} = \mu \cdot \mathbf{H} = \mu_0 \cdot \mu_r \cdot \mathbf{H} \quad (7)$$

$$\mathbf{J} = \sigma \cdot \mathbf{E} \quad (8)$$

where ε_r and μ_r are the relative dielectric permittivity and permeability, respectively.

Finally, in the case of conductor materials, where free charges are present, the current density is obtained by equation (8), which is the local form of the Ohm law; in particular, σ is the electric conductivity.

1.2 Electromagnetic field's equations in sinusoidal regime

A particular case is the one characterized by the sinusoidal regime of the EM field's equations; for example, the electric field component can assume the following shape:

$$E = E_0 \cdot \cos(\omega \cdot t + \varphi) \quad (9)$$

E_0 is the amplitude of the electric field and φ its phase, $\omega = 2\pi f$ is the angular velocity, f is the frequency and T is the period. Using the phasorial form and the same symbol of the real variable, the electric field expression becomes:

$$E = E_0 \cdot e^{j\varphi} \quad (10)$$

The real part of the electric field can be easily obtained:

$$\begin{aligned} E(t) &= \text{Re}[E \cdot e^{j\omega \cdot t}] = \text{Re}[E_0 \cdot e^{j\varphi} \cdot e^{j\omega \cdot t}] = \text{Re}[E_0 \cdot e^{j(\omega \cdot t + \varphi)}] = \\ &= \frac{1}{2} \cdot [E \cdot e^{j\omega \cdot t} + E^* \cdot e^{-j\omega \cdot t}] \end{aligned} \quad (11)$$

This form allows to obtain the Maxwell equations in the frequency domain; considering a linear, isotropic, stationary and homogeneous medium and using the constitutive relations, the EM field equations assume the following form:

$$\nabla \times \mathbf{E} = -j \cdot \omega \cdot \mu \cdot \mathbf{H} \quad (12)$$

$$\nabla \times \mathbf{H} = j \cdot \omega \cdot \varepsilon_c \cdot \mathbf{E} \quad (13)$$

$$\nabla \cdot \mathbf{D} = \rho \quad (14)$$

$$\nabla \cdot \mathbf{H} = 0 \quad (15)$$

$\epsilon_c = \epsilon' - j \cdot \epsilon''$ is the complex dielectric constant, where the real part is the dielectric constant (ϵ') and is related to the material ability to store electric energy, while the imaginary part is the dielectric loss factor (ϵ'') and indicates the dissipation of electric energy due to various mechanisms. If the dissipation is caused by conduction currents (Joule heating), $\epsilon'' = \epsilon_J'' = \sigma/\omega$; in this case, the equation (13) can be recovered by the relation (2):

$$\begin{aligned} \nabla \times \mathbf{H} &= j \cdot \omega \cdot \epsilon \cdot \mathbf{E} + \sigma \cdot \mathbf{E} = j \cdot \omega \cdot \mathbf{E} \cdot \left(\epsilon - \frac{j}{\omega} \cdot \sigma \right) = j \cdot \omega \cdot \mathbf{E} \cdot (\epsilon - j \cdot \epsilon_J'') = \\ &= j \cdot \omega \cdot \epsilon_c \cdot \mathbf{E} \end{aligned}$$

In a general case, $\epsilon'' = \epsilon_J'' + \epsilon_D''$, where ϵ_D'' takes into account different dissipation phenomena (for example, microwave heating); therefore, ϵ_c could be a complex number even if $\sigma \rightarrow 0$.

1.3 Plane waves

Assuming the hypotheses of homogeneous and isotropic medium without losses, the electric field $\mathbf{E}(\mathbf{r}, t)$ satisfies the waves equation in the points identified by the vector \mathbf{r} free of sources (charges and electric and/or magnetic currents):

$$\nabla^2 \mathbf{E}(\mathbf{r}, t) - \mu \cdot \epsilon \cdot \frac{\partial^2 \mathbf{E}(\mathbf{r}, t)}{\partial t^2} = 0 \quad (16)$$

Eq. (16) is easily recovered from eq. (1) written in the time domain:

$$\nabla \times \mathbf{E} = -\mu \cdot \frac{\partial \mathbf{H}}{\partial t} \quad (17)$$

Applying rotor operator to both members of eq. (17), eq. (16) is then obtained considering the following relations:

- the identity: $\nabla \times \nabla \times \mathbf{E} = \nabla(\nabla \cdot \mathbf{E}) - \nabla^2 \mathbf{E}$
- the relation (3) for which $\nabla \cdot \mathbf{E} = 0$ (because $\rho = 0$)
- equation (2) from which: $\nabla \times \mathbf{H} = \epsilon \cdot \frac{\partial \mathbf{E}}{\partial t}$

Considering the particular case of sinusoidal regime with frequency f and angular velocity $\omega = 2\pi f$, the phasor \mathbf{E} satisfies the wave equation in the frequency domain (including the case of medium with losses):

$$\nabla^2 \mathbf{E}(\mathbf{r}) + k^2 \cdot \mathbf{E}(\mathbf{r}) = 0 \quad (18)$$

Eq. (18) can be derived from eq. (1) written in phasorial form:

$$\nabla \times \mathbf{E} = -j \cdot \omega \cdot \mu \cdot \mathbf{H} \quad (19)$$

Applying rotor operator to both members of eq. (19), eq. (18) is then obtained considering the following relations:

- the identity: $\nabla \times \nabla \times \mathbf{E} = \nabla(\nabla \cdot \mathbf{E}) - \nabla^2 \mathbf{E}$
- the relation (3) for which $\nabla \cdot \mathbf{E} = 0$ (because $\rho = 0$)
- equation (2) from which: $\nabla \times \mathbf{H} = j \cdot \omega \cdot \varepsilon_c \cdot \mathbf{E}$

k^2 is related to the medium properties and to the frequency through the dispersion relation:

$$k^2 = \omega^2 \cdot \mu \cdot \varepsilon_c \quad (20)$$

A solution of the wave equation is the plane wave whose electric field can be written in the following form:

$$\mathbf{E}(\mathbf{r}) = E_0 \cdot e^{-j\mathbf{k} \cdot \mathbf{r}} = E_0 \cdot e^{-j\boldsymbol{\beta} \cdot \mathbf{r}} \cdot e^{-\boldsymbol{\alpha} \cdot \mathbf{r}} \quad (21)$$

where: $\mathbf{k} = \boldsymbol{\alpha} + j\boldsymbol{\beta}$; \mathbf{k} is the propagation vector, generally complex, whose squared modulus is equal to (20); $\boldsymbol{\alpha}$ and $\boldsymbol{\beta}$ parameters are the attenuation and the phase constants, respectively.

An interesting case is the uniform plane wave which propagates through a non-dissipative medium, characterized by $\boldsymbol{\alpha} = 0$ and $\beta = \omega \cdot \sqrt{\mu \cdot \varepsilon}$ ($|\mathbf{k}| = k = \beta$), that is:

$$\mathbf{E}(\mathbf{r}) = E_0 \cdot e^{-j\boldsymbol{\beta} \cdot \mathbf{r}} \quad (22)$$

In the case of wave propagation along the “z-axis” ($\boldsymbol{\beta} = \beta \cdot \mathbf{z}_0$), the expression (22) in the time domain can be easily obtained:

$$\mathbf{E}(z, t) = \text{Re} \left[E_0 \cdot e^{-j\beta \cdot z} \cdot e^{j\omega t} \right] = E_0 \cdot \text{Cos}(\omega \cdot t - \beta \cdot z) \quad (23)$$

The wavelength, or spatial period of the wave, is given by the relation:

$$\beta = \frac{2 \cdot \pi}{\lambda} \quad (24)$$

The phase velocity can be obtained differentiating the cosine argument:

$$\beta \cdot dz - \omega \cdot dt = 0 \rightarrow c = \frac{dz}{dt} = \frac{\omega}{\beta} = \frac{\omega}{\omega \cdot \sqrt{\mu \cdot \varepsilon}} = \frac{1}{\sqrt{\mu \cdot \varepsilon}} \quad (25)$$

In the vacuum $c = c_0 = \frac{1}{\sqrt{\mu_0 \cdot \varepsilon_0}}$, where c_0 is the light velocity.

The velocities in the vacuum and in the medium are related by the refraction index, defined as:

$$n = \frac{c_0}{c} = \frac{\sqrt{\mu \cdot \varepsilon}}{\sqrt{\mu_0 \cdot \varepsilon_0}} = c_0 \cdot \sqrt{\mu \cdot \varepsilon} = \sqrt{\mu_r \cdot \varepsilon_r} \quad (26)$$

where μ_r and ε_r are the relative permeability and permittivity, respectively; μ_0 and ε_0 are the free-space permeability and permittivity, respectively.

In the case of non-dissipative media and $\mu \approx \mu_0$, the relation between the velocities in the medium and in the vacuum becomes:

$$c = \frac{1}{\sqrt{\mu \cdot \varepsilon}} = \frac{1}{\sqrt{\mu_0 \cdot \varepsilon_0}} \cdot \frac{\sqrt{\mu_0 \cdot \varepsilon_0}}{\sqrt{\mu \cdot \varepsilon}} = \frac{1}{\sqrt{\mu_0 \cdot \varepsilon_0}} \cdot \frac{\sqrt{\mu_0}}{\sqrt{\mu}} \cdot \frac{1}{\sqrt{\varepsilon_r}} \approx \frac{c_0}{\sqrt{\varepsilon_r}} = \frac{c_0}{n} < c_0$$

being $\varepsilon_r > 0$ and $n = \sqrt{\varepsilon_r} > 0$.

If the medium is dissipative, the wave is attenuated and $\alpha \neq 0$. An interesting case is the uniform plane wave whose attenuation takes place in the same direction of the propagation. Considering the “z-axis” as direction of propagation, the electric field expression in the time domain can be easily recovered:

$$\mathbf{E}(z,t) = \text{Re} \left[E_0 \cdot e^{-j\beta \cdot z} \cdot e^{-\alpha \cdot z} \cdot e^{j\omega t} \right] = E_0 \cdot e^{-\alpha \cdot z} \cdot \text{Cos}(\omega \cdot t - \beta \cdot z) \quad (27)$$

The phase velocity is still equal to: $c = \omega/\beta$; moreover, the relation between α and β parameters and the dielectric permittivity (complex in this case) is not simple like in the previous case.

In particular, the refraction index is complex:

$$n = n' + j \cdot n''$$

The parameters α and β are given by the definition of propagation constant, $\omega^2 \cdot \mu \cdot (\varepsilon' - j \cdot \varepsilon'') = (\alpha + j \cdot \beta)^2$, imposing that the real and the imaginary part are equal and thus obtaining:

$$\alpha = \frac{\omega}{c_0} \left[\frac{\mu_r \cdot \varepsilon_r}{2} \cdot \left(\sqrt{1 + \left(\frac{\varepsilon'}{\varepsilon''} \right)^2} - 1 \right) \right]^{1/2} \quad (28)$$

$$\beta = \frac{\omega}{c_0} \left[\frac{\mu_r \cdot \varepsilon_r}{2} \cdot \left(\sqrt{1 + \left(\frac{\varepsilon'}{\varepsilon''} \right)^2} + 1 \right) \right]^{1/2} \quad (29)$$

1.4 Heat generation

The heat generation which takes place inside a medium subjected to EM radiations can be quantified by an expression deriving from an energy balance equation obtainable through the manipulations of the Maxwell equations.

Under the hypotheses of sinusoidal sources with frequency f , after the transient period, the electric and magnetic fields and the current density are sinusoidal with the same frequency. Therefore, using the phasorial form and introducing the constitutive relations, the Maxwell equations are:

$$\nabla \times \mathbf{E} = -j \cdot \omega \cdot \mu \cdot \mathbf{H} \quad (30)$$

$$\nabla \times \mathbf{H} = \mathbf{J} + j \cdot \omega \cdot \varepsilon_c \cdot \mathbf{E} = (\sigma + j \cdot \omega \cdot \varepsilon_c) \cdot \mathbf{E} = j \cdot \omega \cdot \varepsilon_0 \cdot (\varepsilon'_r - j \cdot \varepsilon''_r) \cdot \mathbf{E} \quad (31)$$

$$\nabla \cdot (\varepsilon \cdot \mathbf{E}) = \rho \quad (32)$$

$$\nabla \cdot (\mu \cdot \mathbf{H}) = 0 \quad (33)$$

The eqs. (30) and (31) in the time domain become:

$$\nabla \times \mathbf{E} = -\mu \cdot \frac{\partial \mathbf{H}}{\partial t} \quad (34)$$

$$\nabla \times \mathbf{H} = \varepsilon_0 \cdot \varepsilon'_r \cdot \frac{\partial \mathbf{E}}{\partial t} + \omega \cdot \varepsilon_0 \cdot \varepsilon''_r \cdot \mathbf{E} \quad (35)$$

The eq. (34) and the eq. (35) have to be multiplied by \mathbf{H} and \mathbf{E} , respectively, and have to be subtracted each other. Finally, reminding that, in general, $\nabla \cdot (\mathbf{A} \cdot \mathbf{B}) = \mathbf{B} \cdot (\nabla \times \mathbf{A}) - \mathbf{A} \cdot (\nabla \times \mathbf{B})$, the following equations is obtained:

$$\frac{\partial}{\partial t} \left(\frac{1}{2} \cdot \epsilon_0 \cdot \epsilon' \cdot \mathbf{E}^2 + \frac{1}{2} \cdot \mu \cdot \mathbf{H}^2 \right) + \nabla \cdot (\mathbf{E} \times \mathbf{H}) = -\omega \cdot \epsilon_0 \cdot \epsilon'' \cdot \mathbf{E}^2 \quad (36)$$

where:

- $\frac{1}{2} \cdot \epsilon_0 \cdot \epsilon' \cdot \mathbf{E}^2 + \frac{1}{2} \cdot \mu \cdot \mathbf{H}^2$ is the EM energy density
- $\mathbf{E} \times \mathbf{H}$ is the Poynting vector (**S**) and represents the flux density of EM energy.
- $-\omega \cdot \epsilon_0 \cdot \epsilon'' \cdot \mathbf{E}^2$ represents the degeneration of EM energy in heat.

Therefore, the instantaneous heat generation is equal to $\omega \cdot \epsilon_0 \cdot \epsilon'' \cdot \mathbf{E}^2$.

From a practical point of view, its the average value in time is useful, and it is given by:

$$\begin{aligned} U_{gen} &= \omega \cdot \epsilon_0 \cdot \epsilon'' \cdot \frac{1}{T} \cdot \int_0^T \mathbf{E}^2 dt = \omega \cdot \epsilon_0 \cdot \epsilon'' \cdot \frac{1}{2} \cdot \text{Re}[\mathbf{E} \cdot \mathbf{E}^*] = \\ &= \omega \cdot \epsilon_0 \cdot \epsilon'' \cdot \frac{1}{2} \cdot |\mathbf{E}|^2 \end{aligned} \quad (37)$$

where: \mathbf{E}^* is the complex conjugate of \mathbf{E} .

So, the heat generation expression has been recovered:

$$U_{gen} = \omega \cdot \epsilon_0 \cdot \epsilon'' \cdot \frac{1}{2} \cdot |\mathbf{E}|^2 \quad (38)$$

According to eq. (38), in order to evaluate the heat generation inside a linear and isotropic medium in stationary and periodic regime, the electric field distribution and the dielectric properties are required.

1.5 Interaction between microwaves and materials

Microwave heating, which uses electromagnetic energy in the frequency range 300-3000 MHz, can be used successfully to heat many dielectric materials. Microwave heating is usually applied at the most popular of the frequencies allowed for ISM (industrial, scientific and medical) applications, namely 915 and 2450 MHz. Domestic microwave ovens are a familiar example operating at 2450 MHz. The way in which a material

will be heated by microwaves depends on its shape, size, dielectric constant and the nature of the microwave equipment used. In the microwave S-band range (2 – 4 GHz), the dominant mechanism for dielectric heating is dipolar loss, also known as the re-orientation loss mechanism. When a material containing permanent dipoles is subject to a varying electromagnetic field, the dipoles are unable to follow the rapid reversals in the field. As a result of this phase lag, power is dissipated in the material.

The conversion of EM energy into heat is related to the loss tangent, defined as the ratio between the loss factor (ϵ'') and the dielectric constant (ϵ'), dependent on frequency and temperature:

$$\operatorname{tg}(\gamma) = \frac{\epsilon''}{\epsilon'} \quad (39)$$

Figure 1.3 shows that water is transparent to microwaves at low frequencies because of the low values of ϵ'' . If salts in solution are present, the phenomenon of conduction losses takes place at frequencies under 1 GHz. The energy dissipation is high in the microwave band, and is due to the mechanism of re-orientation loss, which is maximum at the frequency of 18 GHz. Nevertheless, the latter isn't the operating frequency of the microwaves ovens, which operate at 2.45 GHz, as has been previously pointed out. The reason is related to the penetration depth (δ_p), defined as the depth at which the power drops to 1/e of its value at surface:

$$\delta_p = \frac{1}{\omega \cdot \sqrt{\mu \cdot \epsilon'} \cdot \sqrt{\frac{1 + \left(\frac{\epsilon''}{\epsilon'}\right)^2}{2}}} \quad (40)$$

A very high value of ϵ'' causes a very little penetration depth: the wave is strongly attenuated and heating is localized near the surface. If ϵ'' is very low, the penetration depth is very large: the wave is slightly attenuated and the material is almost transparent to EM radiations. In the latter case the generated power density is negligible.

Therefore, at the frequency of 2.45 GHz there is a compromise between an acceptable penetration depth and an efficient heating process.

Food materials are in general not good electric insulator nor good electric conductors, thus fall into the category of lossy dielectric materials. Both

relative dielectric constants and loss factors of foods are largely influenced by moisture and salt contents, as well as by structure. For instance, the relative dielectric constant of cooked ham for 2450 MHz (72) at room temperature is very close to the value of distilled water, while the relative dielectric loss factor is twice that of free water (23 vs. 10.3). At 2450 MHz, Red Delicious apples with 87.5% moisture content have a relative dielectric loss factor of 11.2, slightly larger than that of free water. Upon removal of moisture content in drying, both relative dielectric constant and loss factors of Red Delicious apples sharply decrease [60].

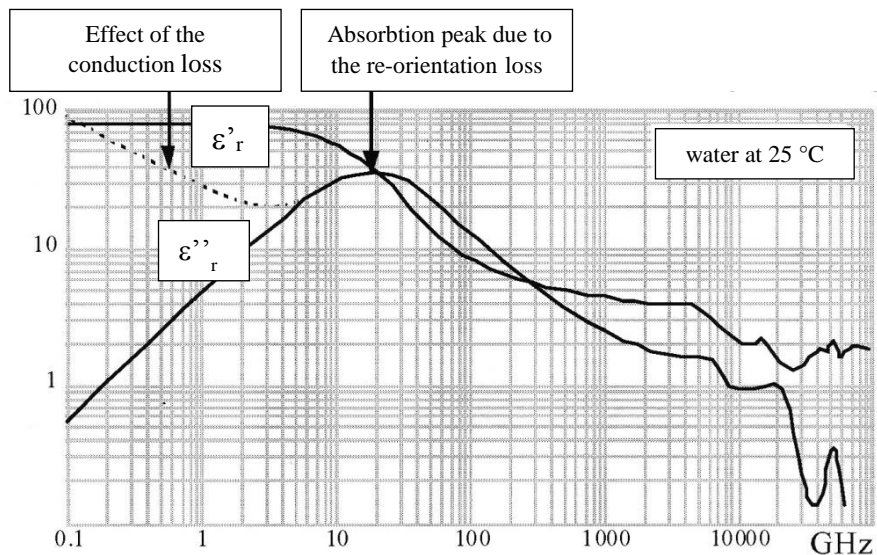


Figure 1.3 Dielectric permittivity of water

CHAPTER 2

Batch tests: apples microwave drying

With the aim of analysing microwave drying processes, a new microwave drying system was developed which can automatically and continuously adjust the power levels by acting on the magnetron duty cycle time in order to control the product temperature. The signal for realizing feedback temperature control was obtained looking inside the illuminated MW chamber by an IR temperature equipment; the latter allowed to detect the instantaneous maximum temperature among the sample slices distributed randomly on the turning table. For the first time the feedback signal was no more related to a single arbitrarily chosen slice inside the MW chamber, which can affect results [33], but to the actual hottest one. Air temperature, humidity and speed were also controlled while the sample-holding turntable was suspended to a technical balance located on the top of the oven for online mass measurement [51]. Considering that microwave drying kinetics mainly depend on moisture diffusion phenomena since external and internal heating resistances become irrelevant to heat transfer mechanism, the ability of realizing experimental drying tests featured by constant temperature levels suggested to process the weight loss data by using a 2D unsteady analytical model for mass diffusion inside isothermal samples. Thus, the effective mass diffusivity [33-35] was determined and, as a consequence, the drying process prediction was allowed [87].

2.1 Experimental set-up

Drying was performed in a pilot plant, Figure 2.1, projected for general purposes in order to encompass different loads, i.e. different materials and samples distributions, weight, size. Hence, it has been aimed that the illuminated cavity could behave as a reverberating chamber, at least in the central space, due to the superposition of multiple modes. A large (with respect to volume where the samples under test were placed) cavity was then required, thus generated microwaves illuminate an insulated metallic cubic chamber (1 m^3). The microwave pilot plant was equipped with a magnetron rated at 2 kW, emitting at a frequency of 2.45 GHz. A mode

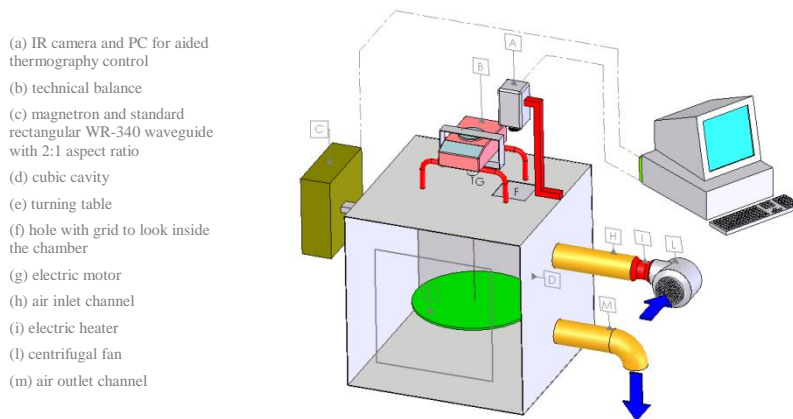


Figure 2.1 Microwave pilot plant heating system

stirrer rotating at 250 rpm was employed to enhance the microwave power distribution inside the cavity.

A teflon rotating tray (50 cm diameter, 22 rpm) housed the samples under test and was connected to a technical balance (Gibertini EU-C 1200 RS) located on the top of the oven. The balance allowed real-time mass measurements. The tray was rotated at 10 rpm on a ball bearing shaft driven by an electrical motor.

An external centrifugal fan facilitated the moisture removal by forcing external air into the cavity; the renewal air flow was kept constant throughout the experiments by controlling the inverter feeding the fan electric motor. The channel feeding the external air flow was equipped with an electric heater controlled by a thermocouple placed on the air expulsion channel. The relative humidities and temperatures both of the exhaust and external air were measured by hygrocipative sensors (BABUC/M, LSI LASTEM Srl). A suitable combination of electric heater power and renewal airflow was selected in order to realize a fixed temperature level inside the illuminated chamber, with a reduced gap (about 10°C) between inlet and ambient air temperatures.

An IR equipment (thermaCAM flir P65) looked inside the oven through a hole 70 mm diameter properly shielded with a metallic grid trespassed by infrared radiation arising from the detected scene but impermeable to high-length EM radiation produced by the magnetron. The camera was

calibrated to account the presence of grid as follows: the temperatures of a large apple slice, cooled from 90 °C to 35 °C, were simultaneously recorded by the IR equipment and by a thermocouple placed on the surface of the target. The emissivity of the target was set to 1, while the air temperatures inside and outside the cavity were set to the same levels adopted during the experiments; thus the reflected ambient temperature was fixed and IR thermography readout was allowed. A second order polynomial related the two measured temperatures.

The measured data, i.e. samples weight, internal and external air temperature, the reflected magnetron energy and duty cycle, were transferred to a personal computer each minute for control and recording purposes. Power control based on thermography temperature readout was accomplished governing an I/O board (AT MIO 16XE50, National Instruments, TX, USA) with a suitably developed Lab View 7.1 code (National Instruments, TX, USA). In particular, the instantaneous maximum temperature in the detected scene was communicated via RS232 to the controlling code each 0.7 seconds.

2.2 Experimental procedure

Preliminary experimental tests were carried on white apples (Golden delicious); their initial moisture content was 86% wet base. Apples were handily peeled, shaped as cylindrical pieces with a diameter of 20 mm, 10

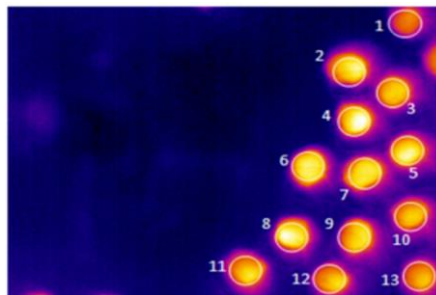


Figure 2.2 Real-time IR thermography for apple slices

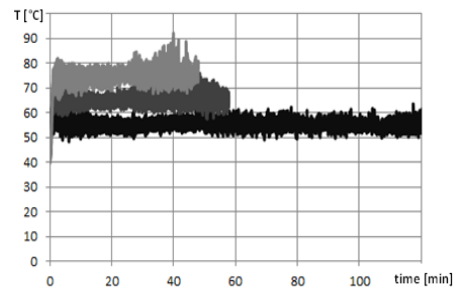


Figure 2.3 Temperature fluctuations for the selected temperature levels

mm height, and finally distributed on the tray. The total amount of samples considered for each trial was 300 g. Weight changes during MW drying were registered on line by the technical balance.

The IR system acquired the instantaneous surface temperature map inside the illuminated cavity gathering in the IR scene a number of samples covering about 20% of total weight (see Figure 2.2). The code scanned for the maximum temperature among the samples appearing in the IR image under test. Because of the turntable rotation, different samples were individuated by analysing different images. Then code automatically adjusted the magnetron delivered power by operating it in intermittent mode with constant power density; an on-off control was then set inside a specified differential band ($\pm 1^\circ\text{C}$) over the target temperature. The code also deliberated the end of the experimental test when the actual moisture content achieved a conventional fixed value of 20%.

Three selected temperature levels were chosen for processing the samples under test, namely 55, 65 and 75 °C; for all of them the internal air temperature was set to 30°C with an air speed equal to 2.5 m/s on the tray layer. The external relative humidity was controlled by an air conditioning system so to realize 6 g_w/kg_a. The renewal air flow was fixed to 25 m³/h in order to contain the inlet temperature excess within few degrees. All the experiments were repeated in triplicates and average values were processed.

2.3 Experimental results

2.3.1 Temperature control during MW heating

The capability of the MW system to keep the controlled temperature during MW drying at the desired values, namely 55, 65 and 75 °C, is shown in Figure 2.3. The average of maximum temperatures recorded on apples' surface was close to the corresponding setpoint values within a difference value of 0.2 °C (Table 2.1). Temperature fluctuations became larger while the process goes on, because of the increase of the power density in the last phase of the drying period due to the mass samples' reduction. In order to quantitatively show the addressed trend, the drying period was divided into two similar parts and the temperatures standard deviations were calculated for these two periods (Table 2.1). The maximum temperature overshoot recorded during the last period of drying at 75 °C was 17.1 °C, thus showing that a product charring could take place and that temperature control became critical at high temperatures and for long time heating. This problem could be overcome by

introducing in MW oven a “mechanical moving mode stirrer” to assure more uniform EM-field distribution.

T [°C]	T _{avg} [°C]	T _{max} -T _{avg} [°C]	T _{min} -T _{avg} [°C]	S.D.	S.D. (I half)	S.D. (II half)
55	55.2	8.9	6.9	1.9	1.9	1.8
65	65.2	11.1	7.6	2.8	2.3	3.2
75	75.1	17.1	9.5	3.1	2.7	3.3

Table 2.1 Set temperatures, averages, temperature oscillations and standard deviations (SD) during first and second half of drying time by microwave of apple slices.

The Figure 2.3 showed that higher the temperature was, higher the temperature oscillations became. This outcome was evidenced evaluating the standard deviations with respect to the corresponding target values, where increasing values were reported for increasing temperatures. Such behaviour could be a consequence of the reduction in dielectric loss factor with temperature increase which requires higher time to keep surface temperature fixed. As a consequence, the instantaneous overall temperature level of the slices increased. The temperature oscillations were not symmetrical if compared to the average temperatures, in particular minimum temperatures (T_{min}) were closer to the corresponding average values than maximum temperatures, (T_{max}). In fact, setting-on the magnetron, the temperature increases took place faster than temperature decreases due to the slower radiative-convective cooling.

2.3.2 Drying curves

Assuming that the measured weight loss was equally distributed for all the samples, it was possible to evaluate the drying curves for the three selected temperature levels. Apple drying curves by hot air and MW, at 55, 65 and 75 °C are shown in Figure 2.4. As expected, apples drying were faster at higher temperatures, with a reduction of drying time that for hot drying was proportional to the increasing of temperature.

MW heating reduced significantly the drying time if compared to convective one. MW absorption provokes internal water heating and evaporation, greatly increasing the internal pressure and concentration gradients and thus the effective water diffusion [18].

Moreover, as reported elsewhere [19], high temperature achieved during the heating cause the solubility of pectic material (apples are rich in

pectins) causing a lowering of rigidity of the cellular tissue, therefore a lower resistance to water transport.

The effect of a temperature increase from 55 to 65 °C reduced to about one half the MW drying time, while the increase from 65 to 75 °C reduced the drying time of only 20%. Probably the higher levels over the temperature set at 75 °C were able to produce a higher pectin gelation phenomena, thus changes in the apple microstructure that delayed the release of water from the matrix to the exterior because of the decrease in porosity or intra-cellular spaces.

Lastly, the slower drying in hot air can be explained recalling that in the convective drying samples temperatures were lower than the air temperature. The gap between air and sample temperatures was always decreasing as the drying process goes on because in the early stages sensible heating dominates, while later the progressive reduction of the evaporation rates was responsible for lower cooling rates. At their best, samples temperatures aimed to the set point values at the very end of the drying process (data not reported). On the opposite, thermal transients featuring MW processing lasted no more than one minute and were hardly appreciable in Figure 2.3.

Apples during MW processing showed typical drying rate, obtained taking the time-derivative of the corresponding curves represented in Figure 2.4. Their behaviour showed the typical trend for fruit drying: after an initial thermal transient, warming up period, when increasing moisture

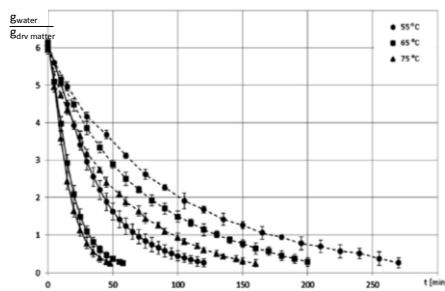


Figure 2.4 Drying curves of apple slices by hot air (dashed line) and microwave (continuous line) heating at 55, 65 and 75 °C.

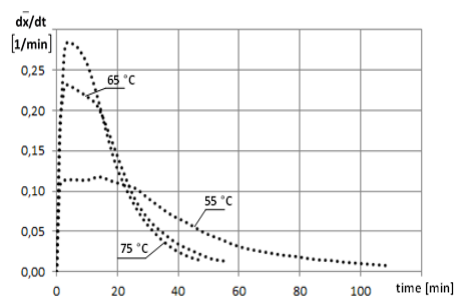


Figure 2.5 Drying rate curves

removal rates were realized, the rate of moisture removal was constant for a short period and then fell off continuously [20]. In warming up period,

microwaves heated without intermittence until the set point temperature was attained. The high content of water (85%) in apples was the main responsible for an efficient internal heat generation causing an increase in product temperature which in turn produced higher diffusion rate. In particular the drying rate curves (Figure 2.5) exhibited a linear (almost adiabatic) increase in evaporated mass; all the curves were first overlapped and then increasing temperatures were responsible for slightly decreasing slopes due to the decrease of the dielectric loss factor and, in turn, to reduced MW absorption. Then, when the internal resistance to transport liquid water to the surface increased, thereby lowering the drying rate, the falling rate period occurred. Hence, internal diffusion may be assumed to be the mechanism responsible for water loss during the drying process. In the last phase of the falling period, since free water content was vanishing, the absorbed MW energy was mainly used to balance convective heat losses from the sample [21]. The thermal conductivity attained its minimum, while at the same time, as a consequence of the mass sample reduction, power densities increased. These occurrences, considering that only surface temperature was controlled, caused the establishment of a temperature gradient inside the sample where the core temperature was greater; thus, the related positive pressure generated inside forced out faster the lasting moisture. While the process further goes on, the addressed phenomena was enhanced considering that higher volumetric heat generation rates were realized.

2.4 The analytical model

Several models have been proposed to describe the rate of water loss during drying processes [22-29]. Among them, the description in terms of the effective diffusivity appears to be more adequate than the ones stemming from empirical kinetics: in fact, the latter don't exhibit a general validity being related to specific load and boundary conditions features [39].

The mass transfer takes place according to the Fick's first law (similar to Fourier law), which relates the diffusive flux to the concentration under the assumption of steady state. It postulates that the flux goes from regions of high concentration to regions of low concentration, with a magnitude that is proportional to the concentration gradient (spatial derivative), or in simplistic terms the concept that a solute will move from

a region of high concentration to a region of low concentration across a concentration gradient. In two or more dimensions, the law is:

$$J = -D \cdot \nabla \Omega \quad (1)$$

where:

- J [kg/(m²·s)] is the "diffusion flux" and measures the amount of substance that will flow through a small area during a small time interval.
- D [m²/s] is the diffusion coefficient or diffusivity
- Ω [kg/m³] is the concentration

Considering eq. (1) and the mass conservation in absence of any chemical reactions, Fick's second law can be derived, thus obtaining an equation analogous to the fundamental equation of conduction heat transfer:

$$\frac{\partial \Omega}{\partial t} = D \cdot \nabla^2 \Omega \quad (2)$$

Usually, when weight loss of dried products is described, the water mass fraction (x) on dry basis is used; the latter parameter is defined as follows:

$$x = m_w/m_s = m_w/(\rho_s \cdot V) = (m_w/V) \cdot (1/\rho_s) = \Omega/\rho_s \quad (3)$$

where:

m_w is the mass of the water; m_s and ρ_s are the mass and the density of the dry matter, respectively; V is the volume of the sample.

Thus, using eq. (3), eq. (2) becomes:

$$\frac{\partial x}{\partial t} = D \cdot \nabla^2 x \quad (4)$$

With the aim of determining the effective diffusivity, the decrease of water in the apple slices has been described through an analytical model based on the local mass balance expressed by eq. (4), assuming isothermal conditions, constant properties, negligible shrinking and cylindrical shapes for samples, Figure 2.6. Considering first type boundary conditions, the dimensionless equations turn out to be:

$$\frac{\partial \mu}{\partial \tau} = \left[\frac{1}{r} \cdot \frac{\partial}{\partial r} \left(r \cdot \frac{\partial \mu}{\partial r} \right) + \frac{R_0^2}{L^2} \frac{\partial^2 \mu}{\partial z^2} \right] \quad (5)$$

$$\mu(z=1, r, \tau) = 0 \quad (6)$$

$$\mu(z, r=1, \tau) = 0 \quad (7)$$

$$\left. \frac{\partial \mu}{\partial z} \right|_{z=0, r} = 0 \quad (8)$$

$$\left. \frac{\partial \mu}{\partial r} \right|_{r=0, z} = 0 \quad (9)$$

$$\mu(z, r, \tau = 0) = 1 \quad (10)$$

where: $\mu(z, r, \tau) = (x(z, r, \tau) - x_e) / (x_0 - x_e)$ is the normalized moisture ratio, x being the mass fraction of the water on dry basis; x_e and x_0 are the unperturbed air and the initial mass fractions of the water in the apple slices; $z = Z/L$ and $r = R/R_0$ are the dimensionless axial and radial coordinates, $2 \cdot L$ and R_0 being the height and the radius of the cylinder, respectively; $\tau = t/t_0$ is the dimensionless time, with $t_0 = R_0^2/D$.

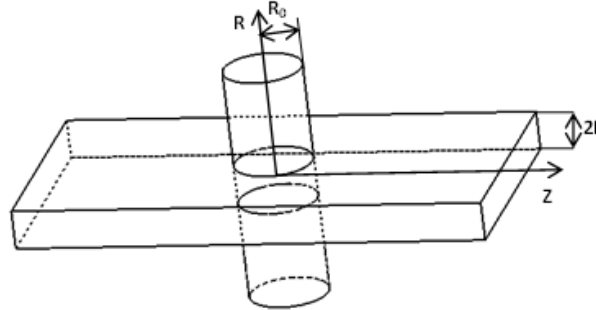


Figure 2.6 Sample geometry

The problem being linear and homogeneous, the solution of the problem may be written as the product of two partial solutions, each one depending on a single spatial coordinate, $\mu(z, r, \tau) = \mu_1(z, \tau) \cdot \mu_2(r, \tau)$. The two partial solutions have to satisfy two distinct problems:

$$\left| \begin{array}{l} \frac{\partial \mu_1}{\partial \tau} = \frac{R_0^2}{L^2} \frac{\partial^2 \mu_1}{\partial z^2} \\ \mu_1(z=1, \tau) = 0 \\ \left. \frac{\partial \mu_1}{\partial z} \right|_{z=0, \tau} = 0 \\ \mu_1(z, \tau=0) = 1 \end{array} \right| \quad \left| \begin{array}{l} \frac{\partial \mu_2}{\partial \tau} = \frac{1}{r} \cdot \frac{\partial}{\partial r} \left(r \cdot \frac{\partial \mu_2}{\partial r} \right) \\ \mu_2(r=1, \tau) = 0 \\ \left. \frac{\partial \mu_2}{\partial r} \right|_{r=0, \tau} = 0 \\ \mu_2(r, \tau=0) = 1 \end{array} \right|$$

Both the two sub-problems are well-known, the former being related to the infinite slab, the latter to the infinite cylinder; they were solved by the separation of variables method yielding:

$$\mu_1(z, \tau) = \sum_{n=1}^{\infty} c_n \cdot G_n(z) \cdot \text{Exp}(-\lambda_n^2 \cdot \tau) \quad (11)$$

$$\mu_2(r, \tau) = \sum_{n=1}^{\infty} d_n \cdot F_n(r) \cdot \text{Exp}(-\beta_n^2 \cdot \tau) \quad (12)$$

where $G_n(z) = \text{Cos}[\lambda_n (L/R_0)z]$ and $F_n(r) = \text{BesselJ}_0(\beta_n \cdot r)$ are the eigen functions and λ_n, β_n are the related eigenvalues arising from the characteristics equations: $\text{Cos}[\lambda_n (L/R_0)] = 0, \text{BesselJ}_0(\beta_n) = 0$.

2.5 Data reduction

Data reduction was carried-on by processing the falling rate period, when the resistance to species transfer by diffusion in the product is much larger than the resistance to species transfer by convection at the surface. Such an occurrence can be shown evaluating the mass transfer Biot number, $\text{Bi} = (h_m L_0)/D$, where h_m is the mass transfer coefficient, L_0 is the reference spatial coordinate. In the case of the air, the mass transfer coefficient can be estimated as $h_m = h/(\rho \cdot c)$, $1/h$ being the thermal resistance to heat transfer, ρ and c being the mass density and the specific heat of the air [31]. The magnitude orders of the reference length and of the mass diffusivity are 10^{-2} and 10^{-9} , respectively, thus the Biot number turns out to be much larger than unity. Accordingly, first type conditions on the wall are properly involved in equations (6) and (7) [32].

On the other hand, the use of the above model including the spatial dependence rather than a concentrated parameters model, was suggested by considering that the time extend needed for the apple moisture content

to decrease from 86 to 20% is small when compared to the sample characteristics time, R_0^2/D .

When performing measurements, it was assumed that the average weight loss for samples under test was described by the above model. Due to the complexity of the response model, the Levenberg Marquadt technique based fitting method has been selected. The technique enables to process non-linear models with an arbitrary number of parameters. Thus, the optimal choice for matching experimental and theoretical data was accomplished by minimizing the *RMSE* merit function:

$$RMSE = \left[\frac{1}{N} \cdot \sum_{i=1}^N (\bar{\mu}(t_i, D) - \bar{\mu}_i)^2 \right]^{1/2} \quad (13)$$

where (μ_i, t_i) are the N experimental normalized moisture content taken at the corresponding times t_i , the function $\bar{\mu}$ is the functional relationship given by the model for the average normalized moisture ratio, D being the unknown diffusivity.

The number of terms in the sum needed to evaluate $\bar{\mu}$ was chosen when the corresponding *RMSE* variation, Δ , was less than 0.001.

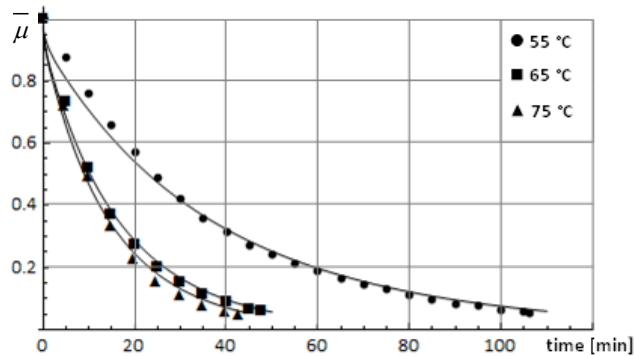


Figure 2.7 Analytical prediction (continuous lines) vs experimental trend (falling rate period)

2.6 Results and discussion

Experimental curves and the corresponding analytical ones resulting from data reduction are reported in Figure 2.7 for the three temperature level at hand. The maximum standard deviation of the experimental data was equal to $0.28 \text{ g}_{\text{water}}/\text{g}_{\text{dry matter}}$.

A satisfying agreement between experimental and analytical data exists and is confirmed by the corresponding correlation coefficients, as shown in Table 2.2. In the same Table, the resulting diffusivities are reported; as expected, the effective mass diffusivity increases with temperature increasing while quantitative results seem to be consistent with the ones reported in literature. In particular, the values of apple effective diffusivities reported by some authors ranges from $1.1 \cdot 10^{-9}$ to $6.4 \cdot 10^{-9}$ depending on airflow and air temperature conditions [35-38]; however, the results presented in this work should be more appropriate since the analytical model holds strictly for isothermal conditions. Such occurrence is closely realized by the present experimental set-up rather than by traditional hot-air heating or by microwave heating without temperature control. In the Table 2.2 are also reported the number of terms needed in the sum and the corresponding RMSE variation.

T [°C]	D [m/s ²]	Terms	RMSE [g _w /g _{dm}]	Δ 10 ⁴	Correlation Coeff.
55 °C	$2.502 \cdot 10^{-9}$	10	0.10932	6.426	0.992
65 °C	$5.601 \cdot 10^{-9}$	16	0.07945	8.821	0.995
75 °C	$6.401 \cdot 10^{-9}$	12	0.14421	8.306	0.991

Table 2.2 Data reduction results

CHAPTER 3

Batch tests on water and oil

Food processing is one of the most successful and largest application of microwaves (MW) since the presence of moisture in the food, which can couple with microwaves easily, facilitates heating thus allowing to realize shorter processing times. On the other hand, the uneven temperature distribution inside the products processed is one of the major obstacle to the diffusion of this technique. This problem can be reduced by acting both on the illuminating system and on target food.

In this chapter, after a brief description of the numerical method on which the software in use is based, the latter is validated through the comparison with the solutions obtained with another software for a simple case. Then, the problem at hand is presented. In particular, thermal response for water and oil samples, placed in a special thermoformed tray, with different size and orientation has been studied. The first aim was to show that temperature predictions can recover experimental results.

Afterwards, uniformity in temperature distribution was investigated by both performing numerical runs and corresponding experimental tests in a pilot plant. With reference to the former approach, samples under test were assumed to be homogeneous dielectric liquid/solid media in which an electromagnetic wave propagates originating dissipative phenomena accounting for energy generation. As a first attempt, natural convection into the samples is neglected in order to test the ability of the mathematical model presented in this study to correctly explain the phenomena of microwave heating within the target. This hypothesis comes true if time measured in the appropriate scale is small. As a further consequence of such hypothesis, cooling by convective/radiative transfer with surroundings is neglected too [86].

3.1. The finite element method

The finite element method (FEM) [62] is a numerical procedure which allows the transformation of analytical equations (for the case at hand, energy balance equations, Maxwell equations and the related boundary conditions) into algebraic equations. The aim is the research of

approximate solutions when there aren't mathematical instruments able to solve the analytical equations exactly. In the specific case, a FEM software, COMSOL Multiphysics [61], has been used; it allows to define, in the pre-processing phase, the physical field of the problem. Then, the geometry is built using the same software or, if available, it is externally built by a CAD software and is imported, imposing the boundary conditions and the constraints. Afterwards, the type of element is chosen and the mesh is generated. The latter depends on the problem at hand. In particular, the elements can be:

- Monodimensionals: problems with a single dependent variable.
- Bidimensionals (triangles or squares) : problems with two dependent variables
- Tridimensionals: (tetrahedra, prisms, hexahedral): problems with three dependent variables

Finally, during the solver phase, the software finds the numerical solution. A number of solvers are available according to the type of problem, stationary or time dependent.

The goodness of the approximated solution has to be checked; in particular, the convergence of the solution depends especially on the shape function and the elements size. So the error drops approaching the nodes, that is reducing the size of the elements; it's necessary to find a compromise between the computational time and the level of discretization: the latter could be increased where needed and elements with a proper shape, compliant with geometry, could be used.

3.2. Comsol vs Ansys HFSS: the software validation

With the aim of validating the software before its use, a simple problem was solved with another FEM software, Ansys HFSS, and the solution was compared with the one obtained by Comsol Multiphysics. As reference, the geometry studied in [63] was assumed. The problem at hand involved a single mode cylindrical microwave cavity, crossed by a

cylinder of still water, whose axis was overlapped to the one of the cavity. The radius of the cavity, the height and the radius of the material load are 63.5 mm, 150 mm and 50 mm, respectively. A magnetron, whose power was set to 1 W, produced microwaves supplied by a rectangular waveguide (WR340), emitting at a frequency of 2.45 GHz. Water dielectric properties were assumed to be independent of temperature; in particular, the real and the imaginary parts of the dielectric permittivity were set to 78 and 9.8, respectively. The geometry was generated in Solidworks ® and was imported in Comsol and in Ansys HFSS (Figure 3.1). For both software, the sampling densities of 6 mm for the water and 17 mm for the air were assumed.

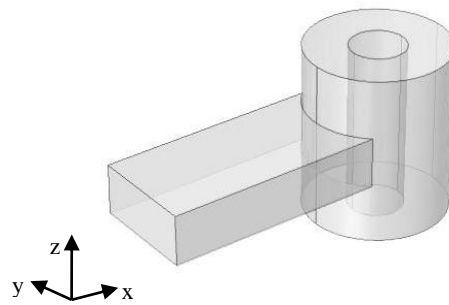


Figure 3.1 Scheme of the single mode cavity

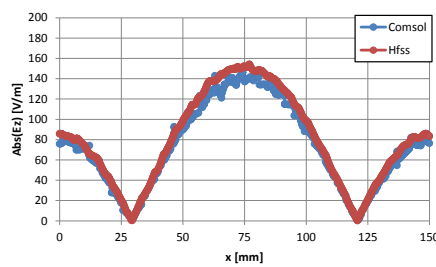


Figure 3.2 Modulus of the “z-component” of the electric field

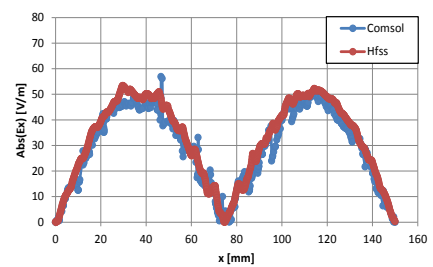


Figure 3.3 Modulus of the “x-component” of the electric field

Figs. 3.2 and 3.3 show the comparison between the component of the electric field along the “z axis” and “x-axis”, while the third component is negligible.

The maximum relative difference between the areas underlay by the curves is equal to 7.4 % for the z-component and to 7.8 % for the x-component. It was verified that, increasing the number of elements, the curves became closer and closer.

Finally, Figure 3.4 shows a bi-dimensional map of the electric field norm generated by Comsol. It's easy to recognize the wave propagation along the waveguide and the different field patterns inside the water and the air.

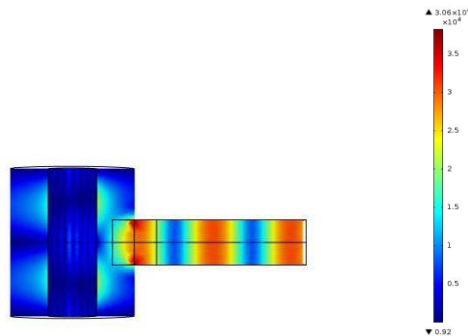


Figure 3.4 Bi-dimensional map of the electric field norm

3.3. Batch tests: the problem at hand

The microwave system used to perform the experiments is schematically represented in Figure 3.5 and its geometry was generated in Solidworks® and was employed for numerical simulations.

In particular, Figure 3.5 is the scheme of a domestic microwave oven (Whirpool MWD302/WH), whose cavity size turns out to be 290x203x285 mm. Samples under test (SUT) are heated by microwaves produced by a magnetron with a nominal power of 900 W and emitting at a frequency of 2.45 GHz. A rectangular (76.5x40.0 mm) waveguide, sealed at one end, is used as a collimator and connects the magnetron to the cavity. Inside the collimator, on the upper side of the waveguide, near the radiating aperture, it is visible a little semisphere which acts to shield the magnetron from back-illumination. The waveguide port opening on

the oven cavity, moreover, exhibits a trapezoidal septum so that it loses the rectangular shape form.

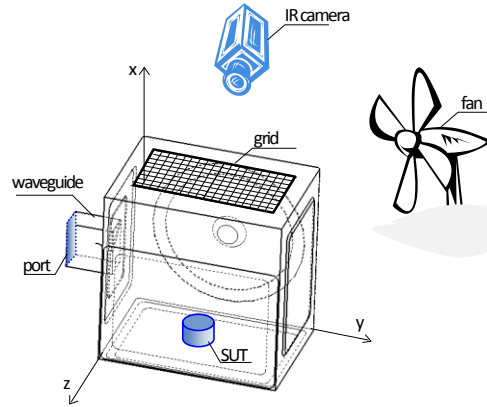


Figure 3.5 Scheme of the experimental setup



Figure 3.6 Experimental set-up

3.3.1 Basic equations

The problem illustrated above is ruled by electromagnetic and heat transfer equations, described in what follows.

Electromagnetic problem

Three-dimensional numerical modelling of batch microwave heating of liquids was carried out by employing the commercial code COMSOL v4.3 [61]. The latter can provide coupling of three physical phenomena, electromagnetism, fluid and energy flow. First, the Maxwell's equations are solved by means of the Finite Element Method (FEM) using unstructured tetrahedral grid cells. Care was taken in choosing a suitable mesh size, according to the criterion expressed in [74]. Then, the electric field distribution \mathbf{E} in the microwave cavity, both for air and for the liquid under test, is determined by imposing:

$$\nabla \times \left(\frac{1}{\mu_r} \nabla \times \mathbf{E} \right) - k_0^2 \left(\varepsilon_r - \frac{i\sigma}{\omega \varepsilon_0} \right) \mathbf{E} = \mathbf{0} \quad (14)$$

where \mathbf{E} is the electric field, ε_r is the relative permittivity, ω is the angular wave frequency, μ_r is the relative magnetic permeability of the material,

k_0 is the wavenumber in vacuum, σ is the electric conductivity. Air and the liquid containers were both supposed completely transparent to microwaves. Assuming negligible resistive material losses, boundary conditions for the Comsol radio frequency module included perfect electric conductors walls for the waveguide and the cavity, i.e. $\mathbf{n} \times \mathbf{E} = 0$, being \mathbf{n} the wall perpendicular unit vector.

Further simplifying assumptions involving the electromagnetic (EM) problem provide:

- materials exhibit linear constitutive laws;
- permeability μ and permittivity ε are temperature independent due to the restricted expected temperature range.

A power of 900 W at 2450 MHz, was supplied through a rectangular TE10 mode waveguide to the cavity.

Continuity boundary condition was set by default for all the interfaces between the confining domains, that is, the container, the cavity and the waveguide. Formally, such condition may be expressed as:

$$\underline{\mathbf{n}} \times (\mathbf{E}_i - \mathbf{E}_j) = \underline{\mathbf{0}} \quad (15)$$

i and j being the domains sharing the interface at hand.

Using the above assumption, volumetric power generation due to microwaves is calculated applying the Poynting power theorem, which yields:

$$U_{\text{gen}} = \frac{1}{2} \omega \varepsilon_0 \varepsilon'' |\mathbf{E}|^2 \quad (16)$$

where ε_0 is the free space permittivity and ε'' is the relative dielectric loss of the material.

Heat transfer problem

The power generation term realizes the coupling of the EM field with the energy balance equation where it represents the “heat source” term. Only the early seconds of the heating process were considered; this time extent turns out to be very small in the proper thermal-time scale. As consequence, natural convection phenomena were neglected and the sample was assumed adiabatic.

In view of the above assumptions and considering constant thermal properties, the energy balance reduces to:

$$\rho c_p \frac{\partial T}{\partial t} = k \nabla^2 T + U_{\text{gen}} \quad (17)$$

where T is the temperature, ρ is the fluid density, c_p is the specific heat, k is the thermal conductivity, t is the time variable, U_{gen} is the specific heat generation.

3.3.2 Experimental set-up

The experimental set-up is shown in Figure 3.6 and is reproduced by the scheme described above and reported in Figure 3.5.

An IR equipment (ThermaCAM flir P65) was employed to look inside the oven through the grid shielding the oven door; the grid was trespassed by infrared radiation arising from the detected scene but was impermeable to high-length EM radiation produced by the magnetron. Of course, the grid presence required a suitable calibration. Samples were placed on the horizontal wall in front of the door, in order to observe the heating patterns of their upper surface by the IR camera. A channel feeding a cooled air flow parallel to the grid plane was employed to keep grid temperature controlled, in order to avoid that unwished grid temperature increases could perturb IR measurements. The liquid media under test was contained in thermoformed trays, whose centre-position was fixed in the middle of the wall, while different orientations were considered, i.e. E-W and N-S, see Figure 3.7.

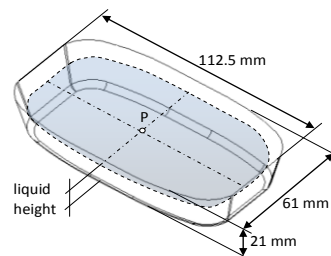


Figure 3.7 The thermoformed tray

3.3.3 Preliminary experimental tests

Preliminary experimental tests were carried out by using the apparatus described above and considering two different tray loads, i.e. 40 and 80 g, both for tap water and oil. Thus, the behaviour of two materials with high-and low dielectric losses has been considered. Each test was configured by setting the tray load and orientation for the selected media. Provided a suitable emissivity calibration, the surface temperature map is

detected by the IR camera. A normalization was carried out in order to suitably compare experimental and analytical maps. Thus, the images represent the dimensionless temperature field defined as: $\theta = (T - T_{\min}) / (T_{\max} - T_{\min})$. The average temperatures were calculated and their standard deviation was assumed as a measure of the uneven surface temperature distribution. The use of normalized temperatures was suggested by considering that they are unaffected by the energy level effectively absorbed by the sample. The latter is varying for each test and hard to measure considering that reflected portion of the radiation is unknown and varies with the load.

In order to check the absence of fluid motion for the selected operating time-intervals, water temperature patterns were compared with corresponding 2% agar gel (solid) solution. The related maps resulted practically the same, thus confirming the expected behaviour. In particular, dimensionless temperature profiles for both water and agar have been extracted along the tray minor axis and compared in Figure 3.8: it is evident that they both recover the same shape thus assuring that no motion is still activated.

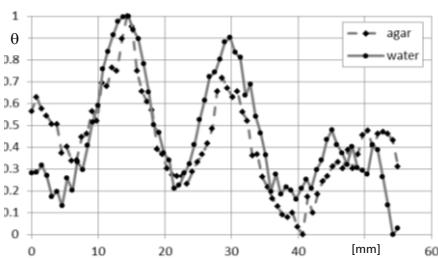


Figure 3.8 Agar vs water θ – profiles along the tray minor axis

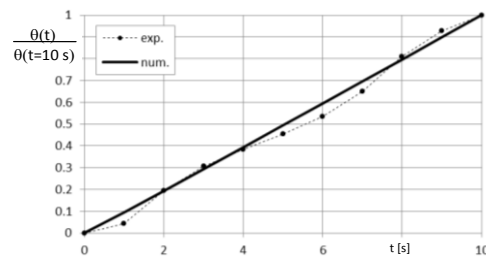


Figure 3.9 Point P temperature evolution

A further check regarded the preliminary validation of adiabatic-sample hypothesis: as expected, in the early stages of the heating process, both numerical and experimental temperatures of the surface centre point, P in Figure 3.7, exhibited a linear temperature increase. This behaviour is witnessed by Figure 3.9 where the dimensionless temperature $\theta(t)/\theta(t=10 \text{ s})$ is represented. The joined- linear behaviour is markedly lost after about 20 s.

3.3.4 Results and discussion

In order to compare the theoretical and the experimental results, numerical simulations were performed considering the same orientations and loads selected for the experiments. The vessel was considered thermally meaningless and the initial temperature was set to 20°.

<i>Material Property</i>	<i>Water</i>	<i>Oil [58]</i>
Heat capacity [J/kg K]	4187	2000
Thermal conductivity [W/m K]	0.7	0.168
Density [kg/m ³]	933	858
Dielectric constant, ϵ'	78	2.80
Dielectric loss, ϵ''	9.8	0.15

Table 3.1 Oil and water properties

In Table 3.1 are listed the values assumed for performing numerical calculations.

Tables 3.2 and 3.3 show the comparison of the predicted and experimental temperature maps for two different orientations of the tray inside the oven. The former is termed horizontal (H) configuration and is featured by orienting the major axis of the tray parallel with the y-axis; the latter, termed vertical (V) configuration, foresees the major axis of the tray parallel with z-axis. In order to promote quantitative comparisons, for each experiment a normalized temperature profile is extracted along the minor or major axis (depending on the thermal contrast it exhibits). It can be seen that the predicted results are in reasonable agreement with experimental results for all the figures, but for water seems more noticeable. Probably, this behaviour can be explained by considering that microwave treatments produced a significantly greater amount in polar compounds in olive oil [59], thus perturbing the original assumed EM properties which, in addition, are more uncertain to select depending on the oil origin.

Some general conclusions can be drawn by analysing the figures. As oil has less dielectric loss, the power absorption in oil samples is in general smaller than water. Power distribution is found to be strongly dependent on H/V-configuration: in fact, the orientation of the vessel plays a critical role on interference of waves, thus, in principle, one can adjust thermal

pattern leading toward to the desired features. Moreover, smaller media layers are featured by higher temperature levels due to larger heat generation rate per unit volume and to the reflection and transmission components at each interface which contribute to a stronger resonance of standing wave inside the sample.

Table 3.2 H-configuration

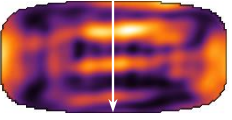
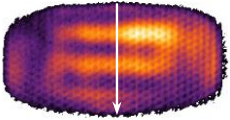
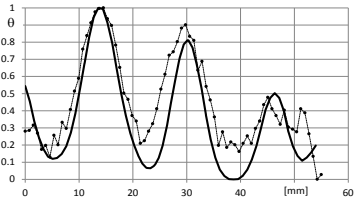
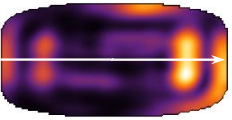
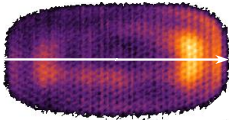
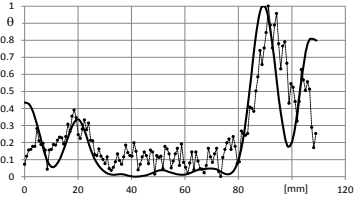
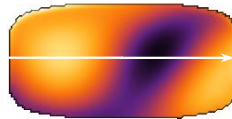
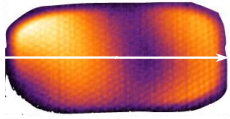
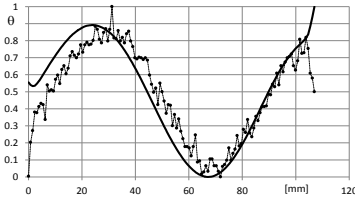
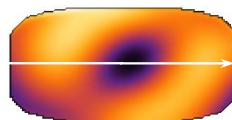
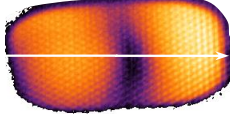
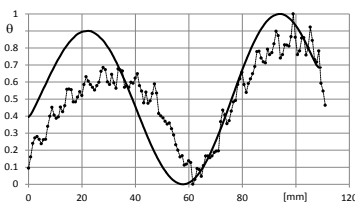
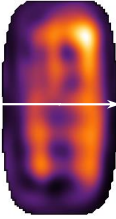
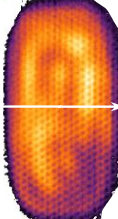
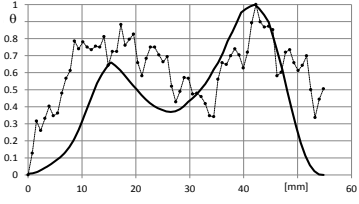
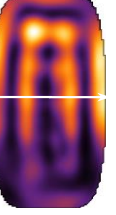
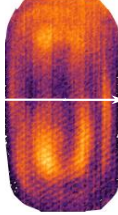
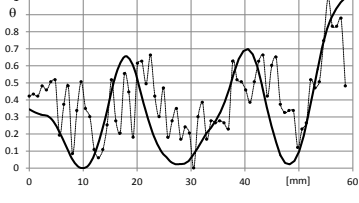

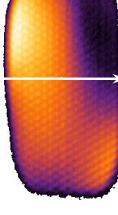
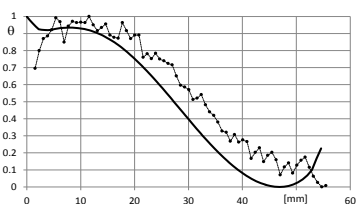
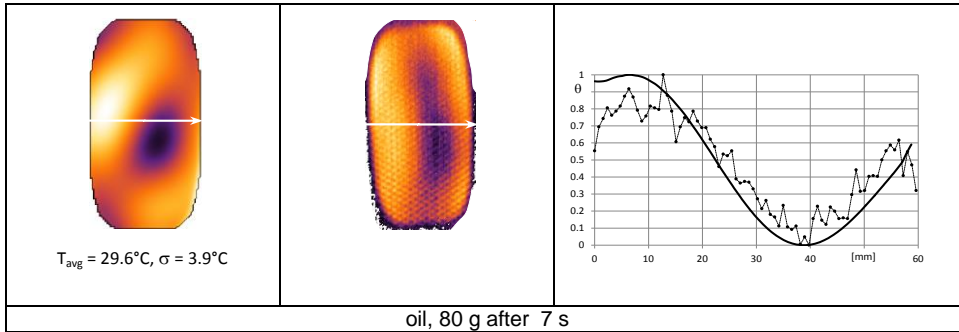
Numerical map	Experimental map	Temperature profiles along the evidenced lines
 <p>$T_{avg} = 28^{\circ}\text{C}$, $\sigma = 5.2^{\circ}\text{C}$</p>		
water, 40 g after 5 s		
 <p>$T_{avg} = 26.7^{\circ}\text{C}$, $\sigma = 6.3^{\circ}\text{C}$</p>		
water, 80 g after 5 s		
 <p>$T_{avg} = 25^{\circ}\text{C}$, $\sigma = 2.5^{\circ}\text{C}$</p>		
oil, 40 g after 7 s		
 <p>$T_{avg} = 27.4^{\circ}\text{C}$, $\sigma = 3^{\circ}\text{C}$</p>		
oil, 80 g after 7 s		

Table 3.3 V-configuration

Numerical map	Experimental map	Temperature profiles along the evidenced lines
 <p data-bbox="517 797 699 819">$T_{avg} = 28.4^{\circ}\text{C}$, $\sigma = 5.7^{\circ}\text{C}$</p>		
water, 40 g after 5 s		
 <p data-bbox="517 1133 699 1155">$T_{avg} = 23.7^{\circ}\text{C}$, $\sigma = 2.7^{\circ}\text{C}$</p>		
water, 80 g after 5 s		
 <p data-bbox="517 1462 699 1485">$T_{avg} = 28.8^{\circ}\text{C}$, $\sigma = 5.3^{\circ}\text{C}$</p>		
oil, 40 g after 7 s		



CHAPTER 4

Continuous flow microwave heating of liquids with constant properties

Among the processes of interest involving microwaves, the pasteurisation of liquids seems to be very promising. Continuous systems have advantages over batch ones with increased productivity, easier clean up, and automation. The flow rate is generally set so that the exit temperature of the fluid in the microwave oven maintains the required temperature in holding section. The temperature of the fluid in the holding section is maintained by external means [56], or in some cases the exit temperature is elevated to a slightly higher level than required to allow for the heat loss through the insulated holding tubes [57].

In this chapter, both a numerical and an analytical model were developed to simulate temperature profiles in continuous laminar pipe flow during microwave heating. The numerical solution was obtained by first solving Maxwell equations and then by coupling them with the energy balance for the flowing fluid. On the other hand, the same problem was solved analytically under the simplifying assumption foreseeing uniform heat generation inside the pipe. With the aim of reducing computational efforts, numerical and analytical results were compared in order to investigate conditions for which the two models allowed to recover the same temperature patterns. Thus, it has been shown that suitable conditions can be found for which the simplified analytical model can lead to an easy way to predict the heat transfer through the pipe [74].

4.1 MW system description

A general purpose pilot plant producing microwaves by a magnetron rated at 2 kW and emitting at a frequency of 2.45 GHz is shown in Figure 4.1; thus, the following models are referred to such an experimental setup. The insulated metallic cubic chamber houses one PTFE applicator-pipe; the pipe is embedded in a box made by a closed-cell polymer foam. The matrix foam was proven to be transparent to microwaves @ 2.45GHz.

The cavity is designed such that its volume is much greater than the applicator-pipe, aiming to approximate a reverberant chamber behaviour.

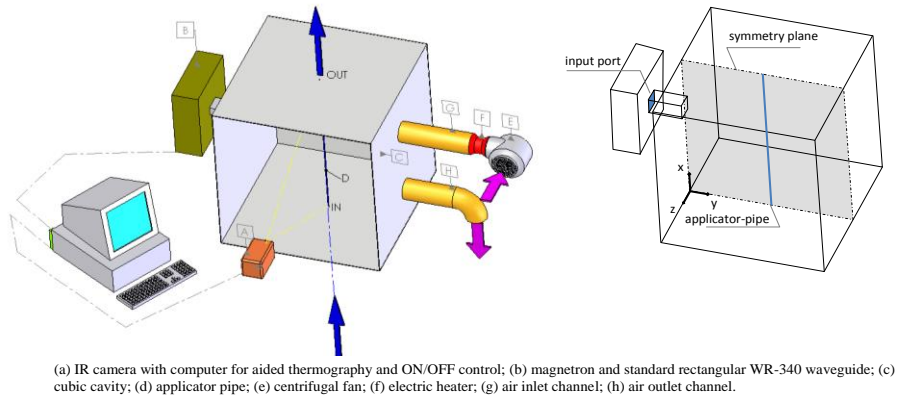


Figure 4.1 Sketch of the available experimental set-up

4.2 Basic equations: the EM problem

Three-dimensional numerical modelling of continuous flow microwave heating was carried out by employing the commercial code COMSOL v4.3 [61]. As already underlined in the previous chapter, the latter can provide the solution of the three physical phenomena, electromagnetism, fluid and energy flow, involved in the problem at hand. First, the Maxwell's equations are solved by means of the Finite Element Method (FEM) [62] using unstructured tetrahedral grid cells; then, the electric field distribution \mathbf{E} in the microwave cavity, both for air and for the applicator-pipe carrying the fluid under process, is determined by imposing:

$$\nabla \times \left(\frac{1}{\mu_r} \nabla \times \mathbf{E} \right) - k_0^2 \left(\varepsilon_r - \frac{i\sigma}{\omega\varepsilon_0} \right) \mathbf{E} = \underline{\mathbf{0}} \quad (1)$$

in which ε_r is the relative permittivity, ω is the angular wave frequency, μ_r is the relative permeability of the material, k_0 is the wavenumber in vacuum, and σ is the electric conductivity.

Air and the PTFE applicator tube were both supposed to be completely transparent to microwaves. Assuming negligible resistive material losses, boundary conditions for the radio frequency module included perfect

electric conductors walls, that is, $\mathbf{n} \times \mathbf{E} = \mathbf{0}$, for the waveguide and the cavity, being \mathbf{n} the local normal vector. At the port, an amount of 2kW EM power, 2450MHz frequency, was supplied through a rectangular TE10 mode waveguide (WR 340).

Continuity boundary condition was set by default for all the interfaces between the confining domains, that is, the pipe, the cavity, and the waveguide. Such condition may be stated as:

$$\mathbf{n} \times (\mathbf{E}_i - \mathbf{E}_j) = \mathbf{0} \quad (2)$$

being i and j the neighbouring discrete portions sharing the interface at hand. Scattering boundary conditions were applied at the inlet and the outlet of the pipe to make the pipe's ends transparent to incoming waves, avoiding that undesired reflected waves travel inward [64].

Due to the symmetry of the problem, and load conditions around the XY plane crossing vertically the oven, the waveguide, and the pipe (see Figure 4.1, right side) the model is reduced to one-half of the device, yielding a more accuracy in the calculation. The condition of perfect magnetic conductor was applied for the surfaces yielding on the symmetry plane:

$$\mathbf{n} \times \mathbf{H} = \mathbf{0} \quad (3)$$

\mathbf{H} being the magnetic field, which has to be therefore parallel to the local normal vector \mathbf{n} on the XY plane.

4.3 Basic equations: the heat transfer problem

In order to obtain the temperature field distribution of liquids flowing in a pipe and subjected to microwaves, the energy balance equation needs the Maxwell equations solution in term of heat generation and the velocity field resulting from Navier-Stokes equations. From a dynamic point of view, two zones are indentified: the "inlet region", whose length is named "dynamic inlet length" (L_{ID}), and the "fully developed region". Under the hypothesis of laminar motion, the parabolic Poiseuille profile is attained after L_{ID} :

$$u(r) = 2 \cdot (1 - r^2) \quad (4)$$

where: $u = U/U_m$ is the dimensionless axial velocity, being U_{av} the mean liquid velocity; $r = R/(D_i/2)$ is the dimensionless radial coordinate, being

R the radial coordinate and D_i the internal pipe diameter. Assuming that the pipe length, before the oven inlet section, is major than L_{ID} , the velocity field will be expressed by eq. (4). The last occurrence allows to simplify the determination of the temperature field, given by the energy balance equation, where the generation term (U_{gen}) is due to microwaves:

$$\rho \cdot c \cdot \left(U \cdot \frac{\partial T}{\partial x} + V \cdot \frac{\partial T}{\partial R} \right) = k \cdot \left[\frac{\partial^2 T}{\partial x^2} + \frac{1}{R} \cdot \frac{\partial}{\partial R} \left(R \cdot \frac{\partial T}{\partial R} \right) \right] + U_{gen} \quad (5)$$

The radial convective term is negligible because the radial component, V , is small respect to the axial component, U . Therefore, the energy balance equation, considering constant flow properties, becomes:

$$\rho \cdot c \cdot U \cdot \frac{\partial T}{\partial x} = k \cdot \left[\frac{\partial^2 T}{\partial x^2} + \frac{1}{R} \cdot \frac{\partial}{\partial R} \left(R \cdot \frac{\partial T}{\partial R} \right) \right] + U_{gen} \quad (6)$$

The power-generation term (U_{gen}) realizes the coupling of the EM field with the energy balance equation where it represents the “heat source” term:

$$U_{gen}(X, Y, Z) = \frac{1}{2} \omega \varepsilon_0 \varepsilon'' |E(X, Y, Z)|^2 \quad (7)$$

already defined in the Chapter 1.

The PTFE tube carrying the fluid exposed to microwave irradiation is considered thermally meaningless. The inlet temperature is set to 10°C, while the remaining boundaries are assumed as adiabatic. Fixed average velocities (namely $U_{av} = 0.02, 0.04, 0.08, 0.16$ m/s) were chosen.

After processing the numerical model, the average spatial value for heat generation was obtained; then, it was used as source term for feeding the analytical solution, described in what follows. Consider that, in practice, such parameter can be measured by calorimetric methods, avoiding numerical calculations, therefore enabling the application of the analytical model with ease.

4.4 Numerical model

A numerical model was developed in COMSOL 4.3 [61] to predict temperature patterns in the fluid continuously heated in a multimode microwave illuminated chamber. The Radio Frequency package, developed for the analysis of propagating electromagnetic waves, was one-way coupled with the Heat Transfer module to solve the energy

balance equation in the thermally developing region. The fluid dynamics problem was considered laminar fully developed, thus velocity profiles were assumed known and parabolic.

4.4.1 Geometry building

The assumed configuration for the system at hand is sketched in Figure 4.1, left side. The pipe carrying the fluid to be heated was 6 mm internal diameter and 0.90 m long. The three dimensional setup was generated in SolidWorks®, providing for symmetrical geometry and load conditions about the XY symmetry plane. Such a choice was performed having in mind to suitably reduce both computational burdens and mesh size while preserving the main aim that is to compare the simplified analytical solution with the numerical one. In particular, a cubic cavity chamber (side-length $L = 0.9$ m) and a standard WR340 waveguide were assumed.

4.4.2 Mesh generation

The available computational domain, reduced by one half as previously specified, was discretized using unstructured tetrahedral grid elements. Special care was devoted in choosing their size, as common sampling criteria may fail under certain circumstances.

According to the Nyquist's criterion, the maximum size of the elements has to be minor than one half of the wavelength [71]:

$$S_{\max} < \frac{\lambda}{2} = \frac{c_0}{2 \cdot f \cdot \sqrt{\mu_r \cdot \epsilon_r}} \quad (8)$$

where the parameters have been defined in the chapter 1.

Some studies (see for instance [68]) suggest that an acceptable criterion for the FEM solution of Maxwell's equations is to use six grids per wavelength; this is more stringent than Nyquist criterion, yet non always satisfying as reported in [74]. In particular, the grid sampling density $N_\lambda = \lambda/\Delta X$ (where ΔX is the grid dimensions) has to be major than 10 in order to obtain an error minor than 1% for the numerical wave phase velocity, considering a simplified case of the homogeneous, lossless 1D Maxwell wave equation, travelling in time t over the X -axis direction.

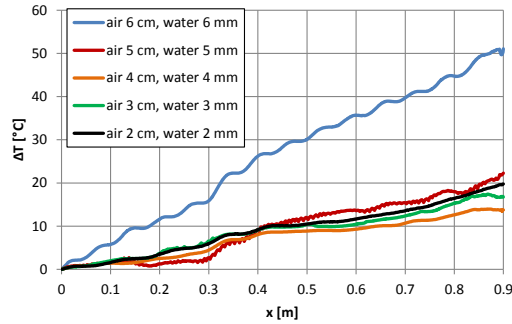


Figure 4.2 Temperature variations of water along the axis of the pipe

Following the indications given by the above simplified assumptions, the sampling density was made increasingly dense in order to evaluate the sensitivity to the elements dimension and to choose the mesh size.

With reference to the geometry described above, several simulations were performed changing the mesh of the two domains, the air and the water.

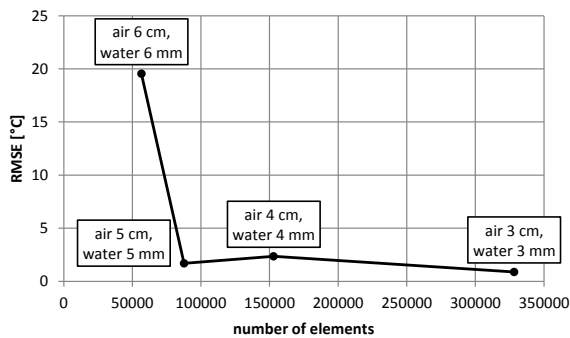


Figure 4.3 RMSE calculated with respect to the reference solution characterized by the maximum sampling density

Figure 4.2 shows the temperature profile along the axis of the pipe corresponding to five simulations: the element size varies from 6 cm to 2 cm for the air and from 6 mm to 2 mm for the water. It clearly appears that there is a great changing when the size of the water elements decreases from 6 mm to 5 mm, and the air one passes from 6 cm to 5 cm. On the other hand, in correspondence of smaller elements there are less sensitive variations. The latter trend has been quantified through the RMSE, shown in Figure 4.3; the latter has been evaluated with respect to the solution characterized by the minor sampling density, that is 2 cm for

the air and 2 mm for the water, being the number of element (about 990000) near the limit of the computer in use.

Since it was considered a grid mesh resolution spacing in the range $0.0107 \div 0.03$ m and $0.002 \div 0.003$ m for the vacuum and water respectively, the limit reported above was strictly satisfied for the moving fluid (i.e. $\lambda_{\text{water}}/\Delta X_{\text{water}} > 30$, λ_{water} being 0.09 m). The same limit is satisfied for the vacuum only where needed.

4.5 Uniform heat generation solution: the analytical model

Aiming to a faster and easier model for continuous microwave heating of liquids, the possibility of recovering the fluid thermal behaviour by an analytical solution has been investigated; uniform heat generation inside the pipe is assumed, retaining the proper average value. This presumption is suggested by supposing that:

- 1) temperature patterns for the flowing fluid are determined by the volume-averaged heat generation, rather than by its local values, as much as the fluid speed increases;
- 2) the illuminated cavity volume is sufficiently large with respect to the applicator-pipe to behave as a reverberating chamber thus reducing uneven EM field patterns.

Conditions, if any, are then searched for which the above assumptions become effective, thus leading to convergence between the simplified-analytical problem and the reference-numerical solution for the temperature field.

In order to evaluate the magnitude order of eq. (6) terms, the following dimensionless variables are introduced:

$$t = \frac{T - T_s}{T_i - T_s}, \quad x = \frac{x}{X_{ref}}, \quad u = \frac{U}{U_{av}}, \quad r = \frac{R}{R_i}$$

where: $t = (T - T_s)/(T_i - T_s)$, is the dimensionless temperature, being T_s and T_i the temperature of the ambient surrounding the tube and the inlet flow temperature, respectively; X_{ref} is the reference length which will be fixed in what follows. Introducing the dimensionless variables into the equation (6), multiplying the same equation by $X_{ref}/(\rho \cdot c \cdot U_{av})$ and dividing by $T_i - T_s$, the following expression is recovered:

$$u \cdot \frac{\partial t}{\partial x} = \frac{\alpha}{U_{av} \cdot X_{ref}} \cdot \frac{\partial^2 t}{\partial x^2} + \frac{4 \cdot \alpha \cdot X_{ref}}{U_{av} \cdot D_i^2} \cdot \frac{1}{r} \cdot \frac{\partial}{\partial r} \left(r \cdot \frac{\partial t}{\partial r} \right) + \frac{U_{gen} \cdot X_{ref}}{(T_i - T_s) \cdot \rho \cdot c \cdot U_{av}} \quad (9)$$

where: $\alpha = k/(\rho \cdot c)$ is the thermal diffusivity, being k the thermal conductivity, r the density and c the specific heat.

Recognizing the Peclet number ($Pe = U_{av} D_i/a$), eq. (9) can be rewritten as follows:

$$u \cdot \frac{\partial t}{\partial x} = \frac{\alpha}{U_{av} \cdot X_{ref}} \cdot \frac{\partial^2 t}{\partial x^2} + \frac{4 \cdot X_{ref}}{P_e \cdot D_i} \cdot \frac{1}{r} \cdot \frac{\partial}{\partial r} \left(r \cdot \frac{\partial t}{\partial r} \right) + \frac{U_{gen} \cdot X_{ref}}{(T_i - T_s) \cdot \rho \cdot c \cdot U_{av}} \quad (10)$$

Imposing that the conduction radial term and the generation term have the same weight of the convection term, the expression of X_{ref} and the dimensionless heat generation (u_{gen}) are obtained:

$$\begin{aligned} \frac{4 \cdot X_{ref}}{P_e \cdot D_i} = 1 & \quad \rightarrow \quad X_{ref} = \frac{P_e \cdot D_i}{4} \\ \frac{U_{gen} \cdot X_{ref}}{(T_i - T_s) \cdot \rho \cdot c \cdot U_{av}} = \frac{u_{gen}}{(T_i - T_s)} \cdot \frac{U_{av} \cdot D_i}{\alpha} \cdot \frac{D_i}{4} \cdot \frac{1}{\rho \cdot c} \cdot \frac{1}{U_{av}} = \\ = \frac{u_{gen} \cdot D_i^2}{4 \cdot k \cdot (T_i - T_s)} = u_{gen} \end{aligned}$$

Introducing the last expressions into eq.(10), eq. (11) is recovered:

$$u \cdot \frac{\partial t}{\partial x} = \frac{4}{P_e^2} \cdot \frac{\partial^2 t}{\partial x^2} + \frac{1}{r} \cdot \frac{\partial}{\partial r} \left(r \cdot \frac{\partial t}{\partial r} \right) + u_{gen} \quad (11)$$

The conductive radial term is negligible, because the value of the Peclet number is high: in fact, considering the field of interest, the velocity is very low and the magnitude order of the cinematic viscosity is 10^{-6} , while the Prandtl number is about 1. Therefore, the energy balance equation is a balance between the axial convection, the radial conduction and the heat generation:

$$u \cdot \frac{\partial t}{\partial x} = \frac{1}{r} \cdot \frac{\partial}{\partial r} \left(r \cdot \frac{\partial t}{\partial r} \right) + u_{gen} \quad (12)$$

The integration of eq. (12) requires two “ r – boundary conditions” and one “ x – boundary condition”:

$$-k \cdot \frac{\partial T(X, R)}{\partial R} \Big|_{R=R_i} = h_e \cdot (T_w(x) - T_s) \quad (13)$$

$$\frac{\partial T(X, R)}{\partial R} \Big|_{R=0} = 0 \quad (14)$$

$$T(0, R) = T_i \quad (15)$$

- The eq. (13) is a third type condition and expresses the continuity of the heat flux at the interface between the wall and the liquid. $T_w(x)$ is the temperature distribution along the wall of the pipe; $1/h_e$ is the thermal resistance of the wall which includes the conductive wall resistance and the tube – ambient one.
- The eq. (14) expresses the symmetry of the temperature profile around the “ x – axis”.
- The eq. (15) expresses the uniformity of the temperature profile at the inlet of the pipe.

Introducing the dimensionless variables into the boundary conditions, the complete dimensionless problem is finally recovered:

$$u \cdot \frac{\partial t}{\partial x} = \frac{1}{r} \cdot \frac{\partial}{\partial r} \left(r \cdot \frac{\partial t}{\partial r} \right) + u_{gen} \quad (16)$$

$$\frac{\partial t}{\partial r} \Big|_{r=1} = -Bi \cdot t(x, 1) \quad (17)$$

$$\frac{\partial t}{\partial r} \Big|_{r=0} = 0 \quad (18)$$

$$t(0, r) = 1 \quad (19)$$

where $Bi = h \cdot (D_i/2)/k$ is the Biot number. Assuming that the pipe is well insulated, as described in the paragraph 4.1, eq. (17) has to be replaced by an adiabatic condition, thus obtaining the following set of dimensionless equations:

$$u \cdot \frac{\partial t}{\partial x} = \frac{1}{r} \cdot \frac{\partial}{\partial r} \left(r \cdot \frac{\partial t}{\partial r} \right) + u_{\text{gen}} \quad (20)$$

$$\left. \frac{\partial t}{\partial r} \right|_{r=1} = 0 \quad (21)$$

$$\left. \frac{\partial t}{\partial r} \right|_{r=0} = 0 \quad (22)$$

$$t(0, r) = 1 \quad (23)$$

The problem being linear, the thermal solution has been written as the sum of two partial solutions:

$$t(x, r) = t_G(x, r) + u_{\text{gen}} \cdot t_V(x, r) \quad (24)$$

The $t_G(x, t)$ -problem represents the solution of the extended Graetz problem featured by a non-homogeneous equation at the inlet and adiabatic boundary condition at wall. On the other hand, the $t_V(x, t)$ -problem takes into account the microwave heat dissipation and includes a non-homogeneous differential equation. Thus, the two partial solutions have to satisfy the two distinct problems expressed in terms of $t_G(x, t)$ and $t_V(x, t)$, respectively:

the Graetz partial solution	the partial solution for heat dissipation
$u \frac{\partial t_G}{\partial x} = \frac{1}{r} \frac{\partial}{\partial r} \left(r \frac{\partial t_G}{\partial r} \right)$	$u \frac{\partial t_V}{\partial x} = \frac{1}{r} \frac{\partial}{\partial r} \left(r \frac{\partial t_V}{\partial r} \right) + 1$
$\left. \frac{\partial t_G}{\partial r} \right _{r=1} = 0$	$\left. \frac{\partial t_V}{\partial r} \right _{r=1} = 0$
$\left. \frac{\partial t_G}{\partial r} \right _{r=0} = 0$	$\left. \frac{\partial t_V}{\partial r} \right _{r=0} = 0$
$t_G(0, r) = 1$	$t_V(0, r) = 0$

Table 4.1 Dimensionless partial problems: uniform heat generation solution

4.5.1 The Graetz problem

The t_G -problem was solved in closed form by the separation of variables method, thus the structure of the solution is sought as follows:

$$t_G(x, r) = \sum_{m=1}^M c_m F_m(r) e^{-\frac{\lambda_m^2 x}{2}} \quad (25)$$

where:

$$F_m(r) = e^{-\frac{r^2 \lambda_m}{2}} \cdot \Lambda \left[\frac{1}{4} (-2 + \lambda_m), r^2 \cdot \lambda_m \right]$$

are the eigen-functions, Λ being the orthonormal Laguerre polynomials and λ_m the related eigenvalues arising from the characteristic equation, $F_m'(1) = 0$. Imposing the initial condition and considering the orthogonality of the eigen-functions, the constants c_m were obtained.

4.5.2 The heat dissipation problem

The “ t_v ”-problem, featured by single non-homogeneous equation, was solved assuming the solution as the sum of two partial solutions:

$$t_v(x, r) = t_1(r) + t_2(x, r) \quad (26)$$

The “ t_1 ”-problem holds the non-homogeneous differential equation, and represents the “ x -stationary” solution. On the other hand, the “ t_2 ”-problem turns out to be linear and homogenous with the exception of the “ x -boundary” condition “ $t_2(0, r) = -t_1(r)$ ”; then, it can be solved by the separation of variables method, recovering the same eigen-functions and eigen-values of the Graetz problem and retaining the same structure of eq. (25):

$$t_2(x, r) = \sum_{m=1}^M b_m F_m(r) e^{-\frac{\lambda_m^2 x}{2}} \quad (27)$$

4.6 Results and discussion

4.6.1 Electromagnetic power generation and cross-section spatial power density profiles

The port input power was set to 2000 W. Due to the high impedance mismatch, as the available cavity was designed for higher loads, the

amount of microwave energy absorbed by the water was 255.7 W, that is 12.8% of the total input power. The corresponding density ranged from $2.6 \cdot 10^3 \text{ W/m}^3$ to $5.83 \cdot 10^7 \text{ W/m}^3$; its distribution along three selected longitudinal paths (namely $R = 0, \pm D_i/2$) is represented in Figure 4.4. In the upper side of the figure, six maps related to sections equally spaced along the pipe length are reproduced. The maps evidence the collocations of the maximum (triangular dot) and minimum (circular dot) values. The fluctuating density profiles exhibit an average period of about 90 mm, for water, and are featured by high radial and axial gradients. As evidenced in Figure 4.4, while moving downstream, maximum and minimum intensities occur at different locations off-centre; the minimum always falls on the edges, while the maximum partially scans the cross tube section along the symmetry axis aiming to the periphery.

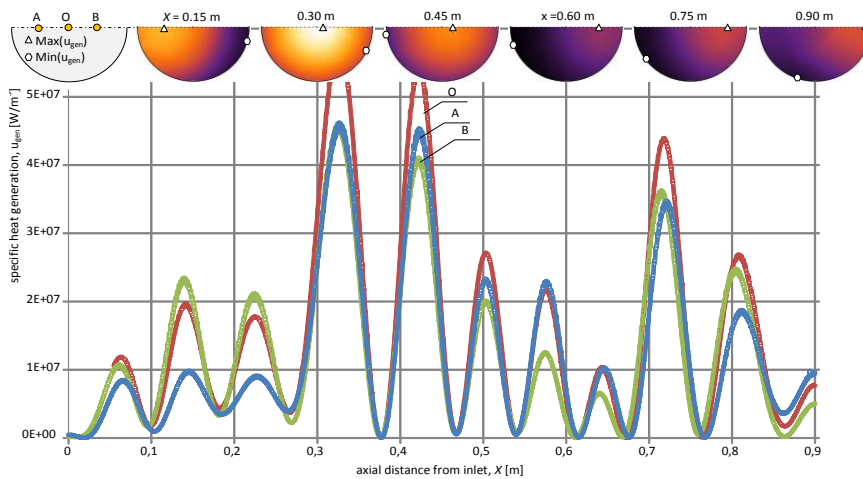


Figure 4.4 Contour plots and longitudinal distributions of specific heat generation U_{gen} along three longitudinal axes corresponding to the points, O (tube centre), A, B.

4.6.2 Comparison between analytical and numerical temperature data

Temperature field resulting from the numerical analysis is sketched in Figure 4.5 for the previously selected six equally-spaced cross sections and for a fixed average velocity, i.e. 0.08 m/s. It is evident that the cumulative effect of the heat distribution turns out into monotonic temperature increase along the pipe axis, irrespective of the driving specific heat generation distribution. Moreover, the temperature patterns

tend to recover an axisymmetric distribution while moving downstream, as witnessed by the contour distribution as well as by the cold spot collocations (still evidenced as circular dots in Figure 4.5), moving closer and closer to the pipe axis. Thus, it is shown that the main hypothesis ruling the analytical model is almost recovered. A similar behaviour is widely acknowledged in the literature [65, 64, 66, 67, 69], that is: 1- temperature distribution appears noticeable even at the tube entrance but it becomes more defined as the fluid travels longitudinally; 2- Higher or lower central heating is observed depending on the ratio between the convective energy transport and MW heat generation. As a further observation, it can be noted that the difference between the extreme temperature values is about $10^{\circ}\text{C} \pm 0.5^{\circ}\text{C}$ almost independently of the section at hand. It seems to be a quite surprising result if one considers that similar differences were realized by employing similar flow rates, pipe geometries and powers in single mode designed microwave cavities, [65, 64]. These latter aimed to reduce uneven heating by applying an electric field with a more suitable distribution providing maximum at the centre of the tube where velocity is high and minimum at the edges where velocity is low.

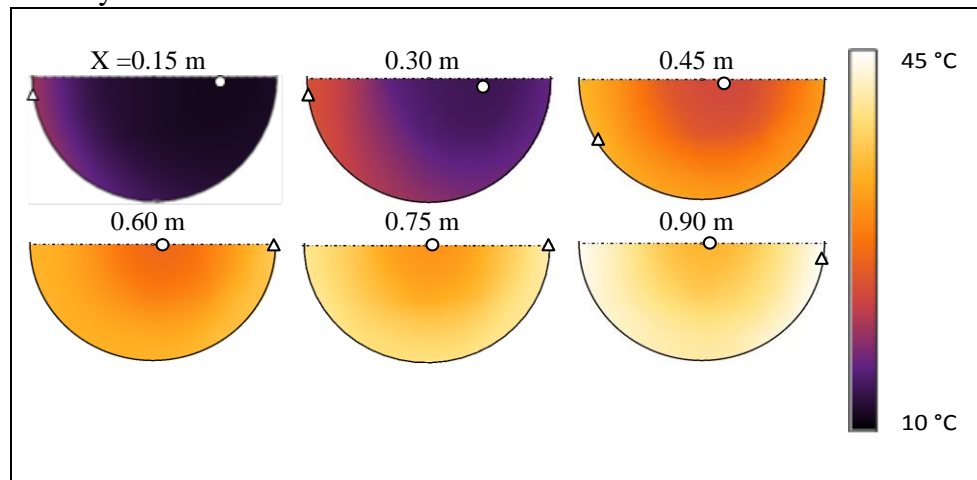


Figure 4.5 Cross sections, equally spaced along the X-axis, of temperature spatial distribution

To clutch quantitative results and compare the analytical and numerical solutions, the bulk temperature seems to be an appropriate parameter;

thus, bulk temperature profiles along the stream are reported in Figure 4.6. A fairly good agreement is attained for increasing velocities: this behaviour can be attributed to the attenuation of the temperature fluctuations related to the shorter heating of the local particles because of the higher flow rates.

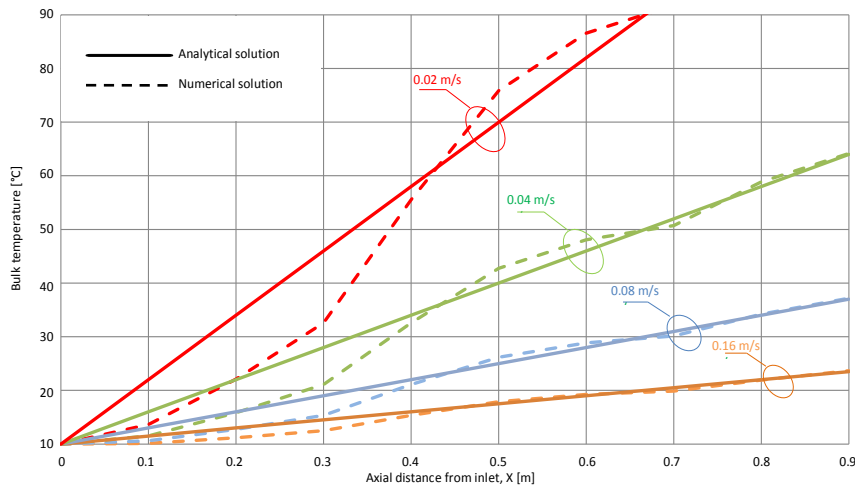


Figure 4.6 Bulk temperature profiles

Radial temperature profiles both for the analytical and numerical solutions are reported in Figure 4.7 for $U_{av} = 0.16$ m/s and 0.08 m/s and for two selected sections, i.e. $X = L/2$ and $X = L$. The analytical solution being axisymmetric, a single profile is plotted vs nine numerical ones taken at the directions evidenced in the lower left corner in Fig. 5, that is shifted of $\pi/8$ rad over the half tube; a cloud of points is formed in correspondence of each analytical profile. Once again, it appears that the dispersion of the numerical-points is more contained and the symmetry is closer recovered for increasing speeds. For the two selected sections and for both velocities, analytical curves underestimate the numerical points around the pipe-axis. Vice versa, analytical predictions tend to overestimate the corresponding cloud-points close to the wall. In any case temperature differences are contained within a maximum of 5.2 °C (attained at the pipe exit on the wall for the lower velocity), thus the analytical and numerical predictions of temperature profiles seem to be in

acceptable agreement for practical applications in the field of food engineering.

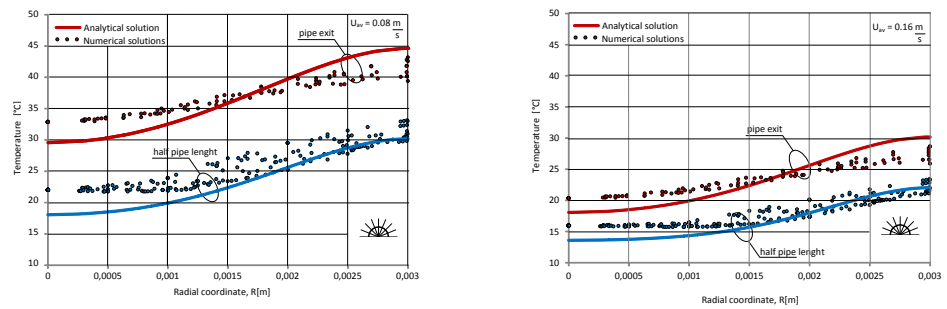


Figure 4.7 Temperature radial profiles

CHAPTER 5

Continuous flow microwave heating of liquids with temperature dependent dielectric properties: the hybrid solution

This chapter proposes a hybrid numerical-analytical technique for simulating microwave (MW) heating of laminar flow in circular ducts, thus attempting to combine the benefits of analytical calculations and numerical field analysis methods, in order to deliver an approximate yet accurate prediction tool for the flow bulk temperature. The main novelty of the method relies on the combination of 3D FEM and analytical calculations, in an efficient thermal model, able to provide accurate results with moderate execution requirements [73].

5.1 Hybrid Numerical-Analytical model definition

The proposed methodology puts together 3D electro-magnetic and thermal FEM results with analytical calculations, for the derivation of the temperature distribution for different flow rates. Numerical approach is used as an intermediate tool for calculating heat generation due to MW heating; the latter distribution, cross section averaged, allows to evaluate the 2D temperature distribution for the pipe flow by an analytical model in closed form. Such a procedure requires a sequential interaction of the analytical and numerical methods for thermal calculations, as illustrated in the flowchart of Figure 5.1 and in the following described.

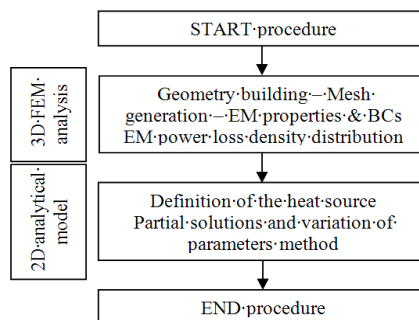


Figure 5.1 Flowchart of the assumed procedure

The developing temperature field for an incompressible laminar duct flow subjected to heat generation is considered. As first step, a 3D numerical FEM model was developed to predict the distribution of the EM field in water continuously flowing in a circular duct subjected to microwave heating. Water is described as an isotropic and homogeneous dielectric medium with electromagnetic properties independent of temperature. Maxwell's equations were solved in the frequency domain to describe the electromagnetic field configuration in the MW cavity supporting the applicator-pipe.

In view of the above hypotheses, the momentum and the energy equations turn out to be coupled through the heat generation term with Maxwell's equations. Then, an approximate analytical solution is obtained considering the effective heat generation distribution arising from the solution of the electromagnetic problem at hand to be replaced by its cross averaged section values; a further improved approximate analytical solution is obtained by considering a suitably weighting function for the heat dissipation distribution. In both cases the proper average value over the water control volume was retained by taking the one arising from the complete numerical solution. The possibility of recovering the fluid thermal behaviour by considering the two hybrid solutions is then investigated in the present work.

5.2 3D Complete FEM Model Description

The models described in this chapter are referred to the experimental set-up sketched in Figure 4.1: a general-purpose pilot plant producing microwaves by a magnetron rated at 2 kW and emitting at a frequency of 2.45GHz. The pipe carrying water to be heated was 8 mm internal diameter (larger than the one modelled in chapter 4) and 0.90m long. Symmetrical geometry and load conditions about the XY symmetry plane are provided. Such a choice was performed having in mind to suitably reduce both computational burdens and mesh size while preserving the main aim that is to compare the two hybrid approximate analytical solution with the numerical one acting as reference. In particular, a cubic cavity chamber (side length, $L = 0.90\text{m}$) and a standard WR340 waveguide were assumed.

The insulated metallic cubic chamber houses one PTFE applicator pipe allowing water continuous flow; the pipe is embedded in a box made by a closed-cell polymer foam, assumed to be transparent to microwaves at 2.45GHz.

A 3D numerical FEM model of the above was developed by employing the commercial code COMSOL v4.3 [61]. It allows coupling electromagnetism, fluid, and energy flow to predict temperature patterns in the fluid continuously heated in a multimode microwave illuminated chamber. The need of considering coupled physics and thus a complete numerical solution (CN), arises by noting that, due to the geometry at hand, no simplified heating distributions can be sought (i.e. the ones based on Lambert Law's) [72]. Ruling equations are solved by means of the finite element method (FEM) using unstructured tetrahedral grid cells. The electric field distribution \mathbf{E} in the microwave cavity, both for air and for the applicator pipe carrying the fluid under process, is determined by imposing eq. (1) of chapter 4.

Temperature distribution is determined for fully developed Newtonian fluid in laminar motion, considering constant flow properties; in such hypotheses, the energy balance reduces to:

$$\rho c_p U \frac{\partial T}{\partial X} = k \nabla^2 T + U_{\text{gen}} \quad (1)$$

where T is the temperature, ρ is the fluid density, c_p is the specific heat, k is the thermal conductivity, X is the axial coordinate, $U(R) = 2U_{\text{av}}(1 - 4R^2/D_i^2)$ is the axial Poiseuille velocity profile, D_i is the internal pipe diameter and R the radial coordinate; U_{gen} is the specific heat generation, i.e. the “electromagnetic power loss density” (W/m^3) resulting from the EM problem. The power-generation term realizes the coupling of the EM field with the energy balance equation where it represents the “heat source” term:

$$U_{\text{gen}}(X, Y, Z) = \frac{1}{2} \omega \varepsilon_0 \varepsilon'' |\mathbf{E}(X, Y, Z)|^2 \quad (2)$$

being ε_0 is the free-space permittivity and ε'' is the relative dielectric loss of the material.

The two-way coupling arises by considering temperature dependent dielectric permittivity [73], whose real and imaginary parts, sketched in Figure 5.2 and Figure 5.3 respectively, are given by the following

polynomial approximations (the subscript “r” used in chapter 1 to indicate the relative permittivity has been omitted):

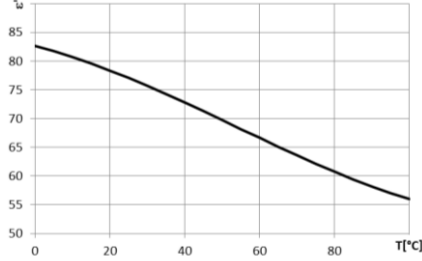


Figure 5.2 Dielectric constant, ε'

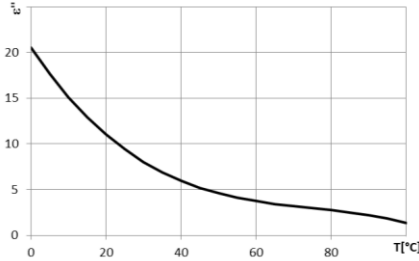


Figure 5.3 Relative dielectric loss, ε''

$$\varepsilon'(T) = -425.963 + 5.16708 \cdot T - 0.0167823 \cdot T^2 + 0.0000171415 \cdot T^3 \quad (3)$$

$$\varepsilon''(T) = -1435.84 + 12.2473 \cdot T - 0.0350158 \cdot T^2 + 0.0000334891 \cdot T^3 \quad (4)$$

5.3 The hybrid solution

5.3.1 The heat generation definition

In this case, the Maxwell's equations are solved first by considering a fixed, temperature independent, dielectric permittivity value. Both the real and imaginary part of the permittivity are selected by evaluating (3) and (4) in correspondence of the arithmetic average temperature T_{avg} arising from the complete numerical solution described in paragraph 5.2. Such a move allows to uncouple the thermal and the EM sub-problems: the power-generation term realizes the one-way coupling of the EM field with the energy balance equation. Considering that the internal pipe diameter is much lower than the pipe length, a simplified cross averaged distribution is sought: its cross averaged value is selected instead, $U_{\text{gen}}(X)$.

A first basic hybrid solution, BH, is obtained by rescaling the $U_{\text{gen}}(X)$ distribution so to retain the overall energy, $U_0 \cdot V$, as resulting from integration of (2) over the entire water volume, V :

$$\hat{U}_{\text{gen,BH}}(X) = \hat{U}_{\text{gen}}(X) \cdot \frac{U_0}{\hat{U}_{\text{gen,avg}}} \quad (5)$$

A further enhanced hybrid solution, EH, is obtained by first weighting and then rescaling $U_{gen}(X)$. In the light of (2), the weighting function is selected as:

$$W(X) = \frac{\varepsilon''[T_b(X)]}{\varepsilon''[T_{b,avg}]} \quad (6)$$

being $T_b(X)$ the bulk temperature corresponding the limiting case of uniform heat generation, U_0 . Finally, the heat dissipation rate for the EH solution is obtained:

$$\hat{U}_{gen,EH}(X) = \hat{U}_{gen}(X) \cdot W(X) \cdot U_0' \quad (7)$$

where U_0' forces the overall energy to be $U_0 \cdot V$. Consider that, in practice, the parameter U_0 can be measured by calorimetric methods, therefore enabling the application of the analytical model with ease. In Figure 5.4 the two different heat generation distributions for the BH and EH problems are reported and compared with the cross section averaged values corresponding to the CN solution. Plots are referred to an arbitrarily selected U_{av} which determines the bulk temperature level of the pipe applicator, $T_{b,avg}$. The CN-curve is practically overlapped to the EH-curve, thus showing a major improvement with respect to the BH-curve.

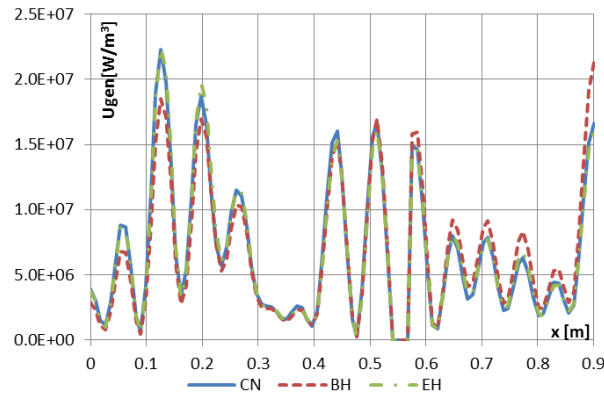


Figure 5.4 Heat generation along the X axis for $U_{av} = 0.08$ m/s

5.3.2 The 2D analytical model

The thermal model provides laminar thermally developing flow of a Newtonian fluid with constant properties and negligible axial conduction.

In such hypotheses, the dimensionless energy balance equation and the boundary conditions in the thermal entrance region turn out to be:

$$2 \cdot (1-r^2) \cdot \frac{\partial t}{\partial x} = \frac{1}{r} \cdot \frac{\partial}{\partial r} \left(r \cdot \frac{\partial t}{\partial r} \right) + u_{\text{gen,H}} \quad (8)$$

$$\left. \frac{\partial t}{\partial r} \right|_{r=1} = 0 \quad (9)$$

$$\left. \frac{\partial t}{\partial r} \right|_{r=0} = 0 \quad (10)$$

$$t(0,r) = 1 \quad (11)$$

where $t = (T-T_s)/(T_i-T_s)$ is the dimensionless temperature, being T_s and T_i the temperature of the ambient surrounding the tube and the inlet flow temperature, respectively; X and R are the axial and radial coordinate; thus, $x = (4 \cdot X)/(Pe \cdot D_i)$ is the dimensionless axial coordinate, with the Peclet number defined as: $Pe = (U_{\text{av}} \cdot D_i)/\alpha$, being α the thermal diffusivity, $r = (2 \cdot R)/D_i$ is the dimensionless radial coordinate; $u_{\text{gen,H}} = (U_{\text{gen,H}} \cdot D_i^2)/(4 \cdot k \cdot (T_i - T_s))$ is the dimensionless hybrid heat generation level, being $U_{\text{gen,H}}$ the corrected heat generation distribution alternatively given by (5) or (7), k the thermal conductivity. The two BH and EH heat generation distributions obtained in the previous section were turned into continuous interpolating function by using the Discrete Fourier Transform:

$$\frac{u_{\text{gen,H}}(x)}{k_1} = 1 + \sum_{n=1}^{N/2} [\beta_n \text{Sin}(n\omega x) + \gamma_n \text{Cos}(n\omega x)] \quad (12)$$

where: $k_1 = (U_0 \cdot D_i^2)/(4 \cdot k \cdot (T_i - T_s))$, $\beta_n = B_n/U_0$ and $\gamma_n = G_n/U_0$, B_n and G_n being the magnitudes of the Sine and Cosine functions; ω is related to the fundamental frequency and N is the number of the discrete heat generation values. The interpolating function of the EH heat generation distribution for $U_{\text{av}} = 0.08$ m/s has been reported in Fig. 6. The expression (12) for the heat generation was used to solve the set of (8) - (11).

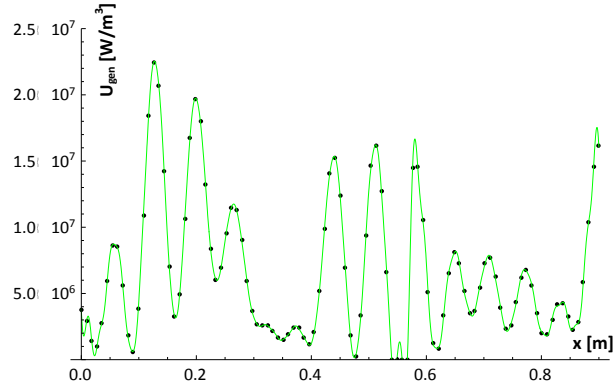


Figure 5.5 Interpolating function (green line) of the EH heat generation distribution (discrete points) for $U_{av} = 0.08$ m/s

The resulting problem being linear, the thermal solution has been written as the sum of two partial solutions:

$$t(x, r) = t_G(x, r) + k_1 \cdot t_V(x, r) \quad (13)$$

The function $t_G(x, r)$ represents the solution of the extended Graetz problem featured by a nonhomogeneous equation at the inlet and adiabatic boundary condition at wall. On the other hand, the function $t_V(x, r)$ takes into account the microwave heat dissipation and exhibits a non-homogeneity in the differential equation. Thus, the two partial solutions have to satisfy the two distinct problems respectively reported in Table 5.1. The Graetz problem was analytically solved following the procedure reported in the paragraph 4.5.1, while the “heat dissipation problem” was solved in closed form by the variation of parameters

The heat dissipation problem with trigonometric heat generation term

The “ t_V ” problem was solved in closed form by the variation of parameters method which allows to find the solution of a linear but non homogeneous problem even if the x -stationary solution does not exist. The solution was sought as:

$$t_V(x, r) = \sum_{j=1}^J A_j(x) \cdot F_j(r) \quad (14)$$

where $F_j(r)$ are the eigen-functions of the equivalent homogeneous problem (obtained from the “ t_V ” problem by deleting the generation term) and are equal to the Graetz problem ones.

the Graetz partial solution	the partial solution for heat dissipation
$u \frac{\partial t_G}{\partial x} = \frac{1}{r} \frac{\partial}{\partial r} \left(r \frac{\partial t_G}{\partial r} \right)$ $\left. \frac{\partial t_G}{\partial r} \right _{r=1} = 0$ $\left. \frac{\partial t_G}{\partial r} \right _{r=0} = 0$ $t_G(0, r) = 1$	$2 \cdot (1-r^2) \frac{\partial t_V}{\partial x} = \frac{1}{r} \frac{\partial}{\partial r} \left(r \frac{\partial t_V}{\partial r} \right) + 1 +$ $+ \sum_{i=1}^{N/2} [\beta_n \sin(n\omega x) + \gamma_n \cos(n\omega x)]$ $\left. \frac{\partial t_V}{\partial r} \right _{r=1} = 0$ $\left. \frac{\partial t_V}{\partial r} \right _{r=0} = 0$ $t_V(0, r) = 0$

Table 5.1 Dimensionless partial problems: BH and EH hybrid solutions

The orthogonality of the eigen-functions respect to the weight $r(1-r^2)$ allowed to obtain the following first order differential equation, which satisfies both the “ t_V ” differential equation and its two “ r ” boundary conditions:

$$\frac{dA_j(x)}{dx} + \frac{1}{2} \lambda_j^2 A_j(x) = f(x) \frac{H_j}{E_j} \quad (15)$$

where

$$E_j = \int_0^1 F_j^2(r) r (1-r^2) dr \quad (16)$$

$$H_j = \int_0^1 \frac{1}{2} r F_j(r) dr \quad (17)$$

$$f(x) = 1 + \sum_{i=1}^{N/2} [\beta_n \sin(n\omega x) + \gamma_n \cos(n\omega x)] \quad (18)$$

Equation (15) was solved imposing the “x” boundary condition of the “tv” problem, which in terms of $A_j(x)$ turns out to be:

$$A_j(0) = 0 \quad (19)$$

In particular, the linearity of the problem suggested to find the functions $A_j(x)$ as the sum of $N/2$ - partial solutions, each one resulting from a simple differential partial equation correlated with the boundary condition:

$$a_{ji}'(x) + \frac{1}{2} \cdot \lambda_j^2 \cdot a_{ji}(x) = \frac{H_j}{E_j}, \quad i = 1 \quad (20)$$

$$\begin{aligned} a_{ji}'(x) + \frac{\lambda_j^2 a_{ji}(x)}{2} = \\ = \frac{H_j}{E_j} \left[\beta_n \sin(n\omega x) + \gamma_n \cos(n\omega x) \right] \quad \text{where } i = 2 \dots N/2 \end{aligned} \quad (21)$$

Finally,

$$a_{ji}(0) = 0 \quad (22)$$

Then, for a fixed value of j , the function $A_j(x)$ turns out to be:

$$A_j(x) = \sum_{i=1}^{N/2} a_{ji}(x) \quad (23)$$

To end with, it was verified that such an analytical solution recovers the corresponding numerical results.

5.4 Results: bulk temperature analysis

Bulk temperature distributions are plotted in Figs. 5.6 - 5.9 for four different inlet velocities, namely 0.008, 0.02, 0.04 and 0.08 m/s. Curves are related to the CN, EH, BH problems and, for reference, a further one evaluated analytically assuming uniform U_0 heat generation (UN). It clearly appears that the EH problem fits quite well the CN problem, whereas the remaining curves underestimate it. In particular, EH and CN curves are almost overlapped for the highest velocity.

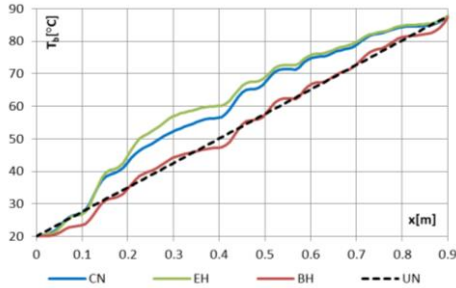


Figure 5.6 Bulk temperature evolution for $U_{av} = 0.008$ m/s

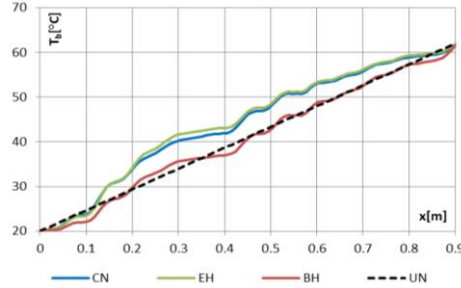


Figure 5.7 Bulk temperature evolution for $U_{av} = 0.02$ m/s

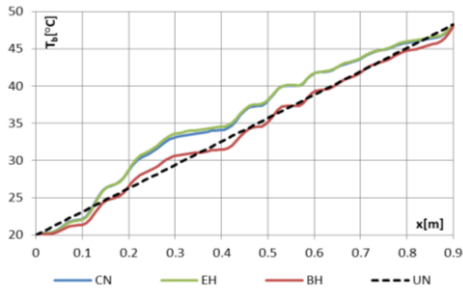


Figure 5.8 Bulk temperature evolution for $U_{av} = 0.04$ m/s

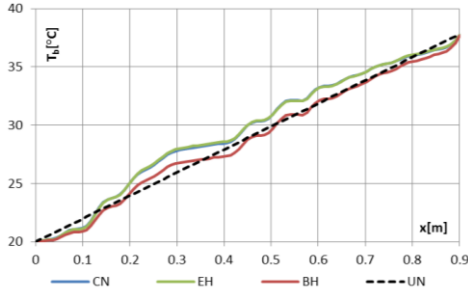


Figure 5.9 Bulk temperature evolution for $U_{av} = 0.08$ m/s

With the aim of evaluating the spatial evolution of the error on the bulk temperature prediction, the percentage error on the bulk temperature prediction has been introduced:

$$err = \frac{T_{b,CN} - T_{b,EH}}{T_{b,CN} - T_i} \quad (24)$$

As can be seen from Figure 5.10, for a fixed value of the axial coordinate the error locally decreases with increasing velocity. For a fixed value of velocity, the error attains a maximum which results to be related to the maximum cumulative error on the prediction of the heat generation distribution. The maximum collocation appears to be independent from velocity, because the BH heat generation is featured by a low sensitivity to the temperature level.

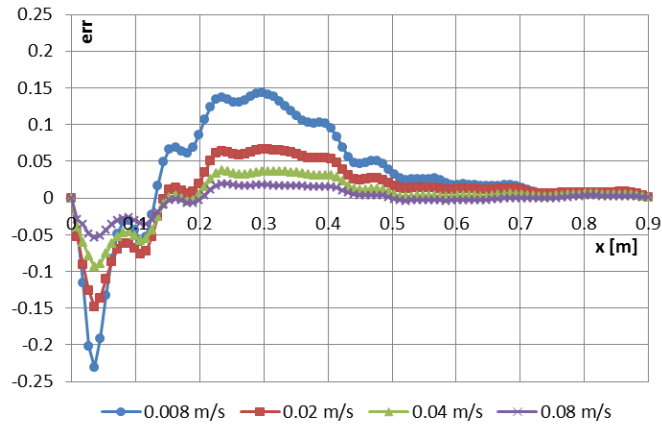


Figure 5.10 Spatial evolution of the error on the bulk temperature prediction

In order to quantitatively compare results, the root mean square error RMSE [$^{\circ}\text{C}$] with respect to the CN solution is evaluated by considering a sampling rate of 10 points per wavelength, see Figure 5.11. For a fixed U_{av} , the RMSE related to the UN and BH curves are practically the same since the BH curve fluctuates around the dashed one, whereas the corresponding EH values turn out to be noticeably reduced.

Interestingly enough, the more is the inlet velocity, the lower is the RMSE. This occurrence is related to the reduced temperature increase which causes the decrease of the dielectric and thermal properties variations along the pipe; moreover, the amplitude of the temperature fluctuations due to the uneven EM field is attenuated for higher flow rates, allowing a more uniform distribution.

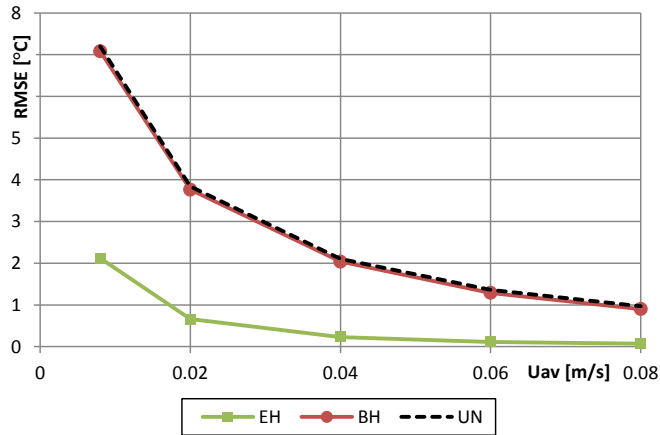


Figure 5.11 Root mean square error with respect to the CN solution

All the calculations were performed on a PC Intel Core i7, 24 Gb RAM. As shown in Table 5.2, the related computational time decrease with increasing speed, since coupling among the involved physics is weaker.

U _{av} [m/s]	Computational time	
	CN	BH
0.008	12 h, 48 min, 20 s	21 min, 11 s
0.02	9 h, 21 min, 40 s	22 min, 16 s
0.04	5 h, 49 min, 41 s	22 min, 9 s
0.08	4 h, 18 min, 16 s	22 min, 9 s

Table 5.2 Computational time for CN and BH solutions

Of course, no meaningful variations are revealed for the BH problem where the time needed was roughly 22 min for each speed. Thus a substantial reduction was achieved this being at least one tenth.

CHAPTER 6

Quantitative IR Thermography for continuous flow microwave heating

6.1 Theory of thermography

In order to measure the temperature of the liquid flowing in the pipe during MW heating process and to evaluate the goodness of the theoretical models prediction, experiments were performed using an infrared radiometer. In particular, the equation used by the radiometer was manipulated to overcome the problems related to the presence of the grid between the camera and the target [85].

With the aim of introducing the equations used in this chapter, a brief description about the infrared radiations and the fundamental equation of infrared thermography are presented.

6.1.1 The infrared radiations

Thermography makes use of the infrared spectral band, whose boundaries lie between the limit of visual perception, in the deep red, at the short wavelength end and the beginning of the microwave radio band, at the long-wavelength end (Figure 1.1).

The infrared band is often further subdivided into four smaller bands, the boundaries of which are arbitrarily chosen. They include: the near infrared (0.75 - 3 μm), the middle infrared (3 - 6 μm) and the extreme infrared (15 - 100 μm).

6.1.2 Blackbody radiation

A blackbody is defined as an object which absorbs all radiation that impinges on it at any wavelength.

The construction of a blackbody source is, in principle, very simple. The radiation characteristics of an aperture in an isotherm cavity made of an opaque absorbing material represents almost exactly the properties of a blackbody. A practical application of the principle to the construction of a

perfect absorber of radiation consists of a box that is absolutely dark inside, allowing no unwanted light to penetrate, except for an aperture in one of the sides. Any radiation which then enters the hole is scattered and absorbed by repeated reflections so only an infinitesimal fraction can possibly escape. The blackness which is obtained at the aperture is nearly equal to a blackbody and almost perfect for all wavelengths.

By providing such an isothermal cavity with a suitable heater it becomes what is termed a cavity radiator. An isothermal cavity heated to a uniform temperature generates blackbody radiation, the characteristics of which are determined solely by the temperature of the cavity. Such cavity radiators are commonly used as sources of radiation in temperature reference standards in the laboratory for calibrating thermographic instruments, such as FLIR Systems camera used during the experimental tests.

Now consider three expressions that describe the radiation emitted from a blackbody.

Planck's law

Max Planck was able to describe the spectral distribution of the radiation from a blackbody by means of the following formula:

$$I_{\lambda,b}(T) = \frac{2 \cdot C_1}{\lambda^5 \cdot \left[\text{Exp}\left(\frac{C_2}{\lambda \cdot T}\right) - 1 \right]} \left[\frac{\text{W}}{\text{m}^2 \cdot \mu\text{m} \cdot \text{sterad}} \right] \quad (1)$$

where: the wavelengths are expressed by μm ; $C_1 = h \cdot c_0^2 = 0.59 \cdot 10^8$ [$\text{W}(\mu\text{m}^4)/\text{m}^2$], $h = 6.62 \cdot 10^{-34}$ being the Planck constant; $C_2 = h \cdot c_0/k = 1.439 \cdot 10^4$ [$\mu\text{m} \cdot \text{K}$], $k = 1.38 \cdot 10^{-23}$ J/K being the Boltzmann constant.

Planck's formula, when plotted graphically for various temperatures, produces a family of curves (Figure 6.1). Following any particular curve, the spectral emittance is zero at $\lambda = 0$, then increases rapidly to a maximum at a wavelength λ_{max} and after passing it approaches zero again at very long wavelengths. The higher temperature, the shorter the wavelength at which the maximum occurs.

Wien's displacement law

By differentiating Planck's formula with respect to λ , and finding the maximum, the Wien's law is obtained:

$$\lambda_{\max} \cdot T = 2897.8 = C_3 \quad [\mu\text{m} \cdot \text{K}] \quad (2)$$

The sun (approx.. 6000 K) emits yellow light, peaking at about 0.5 μm in the middle of the visible spectrum.

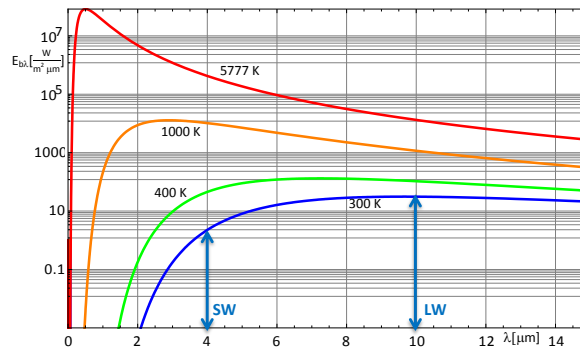


Figure 6.1 Planck's curves plotted on semi-log scales

At room temperature (300 K) the peak of radiant emittance lies at 9.7 μm in the far infrared, while at the temperature of liquid nitrogen (77 K) the maximum of the almost insignificant amount of radiant emittance occurs at 38 μm , in the extreme infrared wavelengths.

Stefan Boltzmann's law

By integrating Planck's formula on the hemisphere of solid angle 2π and from $\lambda = 0$ to $\lambda = \infty$, the total radiant emittance is obtained:

$$E_b(T) = \sigma \cdot T^4 \quad [\text{W}/\text{m}^2] \quad (3)$$

where: σ is the Stefan-Boltzmann constant. Eq. (3) states that the total emissive power of a blackbody is proportional to the fourth power of its absolute temperature. Graphically, $E_b(T)$ represents the area below the Planck curve for a particular temperature.

6.1.3 Non-blackbody emitters

Real objects almost never comply with the laws explained in the previous paragraph over an extended wavelength region, although they may approach the blackbody behaviour in certain spectral intervals.

There are three processes which can occur that prevent a real object from acting like a blackbody: a fraction of the incident radiation α may be absorbed, a fraction ρ may be reflected, and a fraction τ may be transmitted. Since all of these factors are more or less wavelength dependent

, the subscript λ is used to imply the spectral dependence of their definitions. The sum of these three factors must always add up to the whole at any wavelength, so the following relation has to be satisfied:

$$\alpha_{\lambda} + \rho_{\lambda} + \tau_{\lambda} = 1 \quad (4)$$

For opaque materials $\tau_{\lambda} = 0$ and the relation simplifies to:

$$\alpha_{\lambda} + \rho_{\lambda} = 1 \quad (5)$$

Another factor, called emissivity, is required to describe the fraction ε of the radiant emittance of a blackbody produced by an object at a specific temperature. Thus, the spectral emissivity is introduced, which is defined as the ratio of the spectral radiant power from an object to that from a blackbody at the same temperature and wavelength:

$$\varepsilon_{\lambda} = \frac{E_{\lambda}}{E_{\lambda b}} \quad (6)$$

Generally speaking, there are three types of radiation source, distinguished by the ways in which the spectral emittance of each varies with wavelength:

- a blackbody, for which $\varepsilon_{\lambda} = \varepsilon = 1$
- a graybody, for which $\varepsilon_{\lambda} = \varepsilon = \text{constant less than 1}$
- a selective radiator, for which ε varies with wavelength

According to the Kirchhoff's law, for any material the spectral emissivity and spectral absorptance of a body are equal at any specified temperature and wavelength, that is:

$$\varepsilon_{\lambda} = \alpha_{\lambda} \quad (7)$$

Considering eqs. (5) and (7), for an opaque material, the following relation can be written:

$$\varepsilon_{\lambda} + \rho_{\lambda} = 1 \quad (8)$$

6.1.4 The fundamental equation of infrared thermography

When viewing an object, the camera receives radiation not only from the object itself. It also collects radiation from the surrounding reflected via the object surface. Both these radiations contributions become attenuated to some extent by the atmosphere in the measurement path. To this comes a third radiation contribution from the atmosphere itself (Figure 6.2).

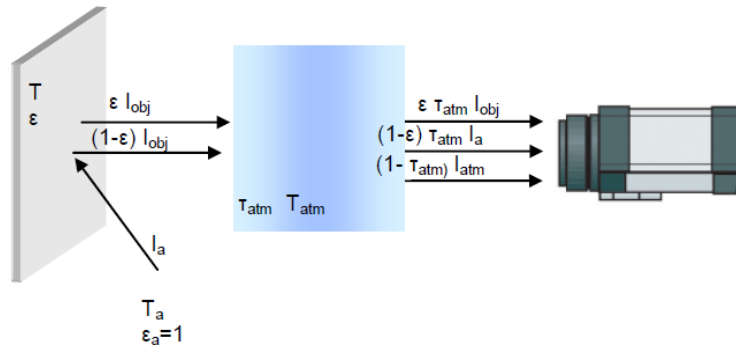


Figure 6.2 Schematic representation of the general thermographic measurement situation

Assume that the received radiation power, quantified by the blackbody Plank function I , from a blackbody source of temperature T_{source} generates a camera output signal S that is proportional to the power input. In particular, the target radiance is given by the following equation [88]:

$$I(T_{\text{app}}) = \varepsilon \cdot \tau_{\text{atm}} \cdot I(T_{\text{targ}}) + (1 - \varepsilon) \cdot \tau_{\text{atm}} \cdot I(T_{\text{refl}}) + (1 - \tau_{\text{atm}}) \cdot I(T_{\text{atm}}) \quad (9)$$

In the right side of eq.(9) there are three contributions:

1. *Emission of the object*: $\varepsilon \cdot \tau_{\text{atm}} \cdot I(T_{\text{targ}})$, where ε is the emissivity of the object and τ_{atm} is the transmittance of the atmosphere; T_{targ} is the temperature of the target.
2. *Reflected emission from ambient sources*: $(1 - \varepsilon) \cdot \tau_{\text{atm}} \cdot I(T_{\text{refl}})$ where $\rho = 1 - \varepsilon$; T_{refl} is the temperature of the ambient sources.
3. *Emission from the atmosphere*: $(1 - \tau_{\text{atm}}) \cdot I(T_{\text{atm}})$, where $(1 - \tau_{\text{atm}})$ is the emissivity of the atmosphere; T_{atm} is the temperature of the atmosphere.

In the left side of eq. (9) there is the total target radiance measured by the radiometer, which is a function of the apparent temperature of the target

(T_{app}); the latter parameter can be obtained setting ε to 1. Consider that τ_{atm} can be assumed equal to 1 in the most of applications.

Commonly, during infrared measurements, the operator has to supply all the parameters of eq. (9) except T_{targ} , which becomes the output of the infrared measurements.

In order to explicit the temperature dependence of the function I , the differentiation of eq. (1) is required; this move leads to the following expression:

$$\frac{dI/I}{dT/T} = \frac{C_2}{z} \cdot \frac{\text{Exp}[c_2/z]}{\text{Exp}[c_2/z]-1} \quad (10)$$

where $z = \lambda \cdot T$. Moreover, a new coefficient n can be introduced, which links I and T :

$$I \approx T^n \rightarrow \ln(I) = n \cdot \ln(T) \rightarrow \frac{dI}{I} = n \cdot \frac{dT}{T} \quad (11)$$

There are two different occurrences:

$$1) \quad z < \lambda_{\text{max}} \cdot T \rightarrow \frac{dI/I}{dT/T} \approx \frac{c_2}{z} \quad (12)$$

In this case, comparing the expressions (11) and (12), the following result is recovered:

$$n = C_2/z \approx 5 \cdot C_3/z = 5 \cdot \lambda_{\text{max}}/\lambda \rightarrow \text{error} < 1\%, \text{ if } \lambda < \lambda_{\text{max}}$$

$$2) \quad z > \lambda_{\text{max}} \cdot T \rightarrow \frac{dI/I}{dT/T} = n \approx 1 + 2.5 \cdot \frac{\lambda_{\text{max}}}{\lambda} \quad (13)$$

Finally, the approximation of I is resumed as follows:

$$\begin{cases} I \approx T^5 & \text{if } \lambda_{\text{max}} = \lambda \\ I \approx T^n & \text{with } n = \begin{cases} 5/\lambda^*, & \text{if } \lambda^* \leq 2.5 \\ 1 + 2.5/\lambda^*, & \text{if } \lambda^* > 2.5 \end{cases} \end{cases} \quad (14)$$

where $\lambda^* = \lambda/\lambda_{\text{max}}$.

The radiometers work at a fixed wavelength lying in the “shortwave (SW) window” (3 – 5 μm) or in the “longwave (LW) window” (7 – 14 μm),

where the atmosphere can be assumed transparent to the infrared radiations.

The shortwave radiometers at ambient temperature detect less energy, but are more sensitive to temperature variations (Figure 6.1).

Typical values of n are the followings:

$$\lambda_{SW} \approx 4 \mu\text{m} \rightarrow n \approx 12.5$$

$$\lambda_{LW} \approx 10 \mu\text{m} \rightarrow n \approx 5$$

6.2 Experimental set-up

Experiments were performed in a microwave pilot plant, Figure 6.3, intended for general purposes in order to encompass different loads, i.e. different materials and samples distributions, weight, size. Microwaves were generated by a magnetron rated at 2 kW nominal power output and operating at a frequency of 2.4 GHz. A rectangular WR340 waveguide connects the magnetron to the cavity. Microwaves illuminated an insulated metallic cubic chamber (0.9 m side length) housing the pyrex (MW transparent) glass applicator pipe (8 mm inner diameter, 1.5 mm thick) carrying water continuous flow to be heated.

The inner chamber walls were insulated by polystyrene slabs black painted. The pipe was placed inside the chamber in such a way that its longitudinal axis lied down along a symmetry plane due to both geometry and load conditions. Such a choice was realized having in mind to suitably reduce computational efforts, as previously explained.

A circulating centrifugal pump drawn out water from a thermostatic bath to continuously feed the applicator-pipe with a fixed inlet temperature. The flow rate was accurately tuned by acting on an inverter controlling the pump speed. The liquid leaving the cavity was cooled by a heat exchanger before being re-heated by the thermostatic control system in order to obtain the previous inlet temperature, thus realizing a closed loop.

A centrifugal fan facilitated the air removal by forcing external air into the cavity; the renewal air flow was kept constant throughout the experiments in order to stabilize the heat transfer between the pipe and the environment. The channel feeding the external air flow was equipped with an electric heater controlled by the feedback from a thermocouple in order to realize a fixed temperature level for the air inside the illuminated chamber, that is 30°C.

A fan placed inside the MW chamber, connected by its shaft to an external electric motor, was used to make uniform the temperature distribution.

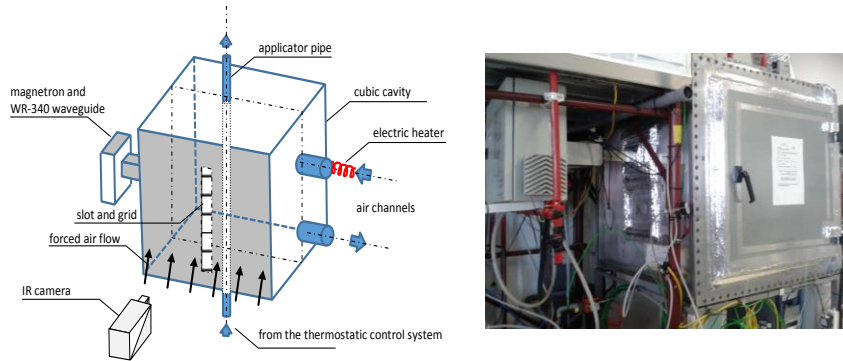


Figure 6.3 Sketch and picture of the available MW pilot plant

A longwave IR radiometer, thermaCAM by Flir mod. P65, looked at the target pipe through a rectangular slot 30 mm x 700 mm properly shielded with a metallic grid trespassing by infrared radiation arising from the detected scene (less than 15 μm wavelength for what of interest) but being sealed for high-length EM radiation produced by the magnetron (12 cm wavelength). Finally, a further air flow was forced externally, parallel to slot holding the grid in order to establish its temperature to $24 \pm 0.5^\circ\text{C}$.

6.3 Temperature readout procedure

The presence of the grid is a major obstacle wishing to perform temperature-readout when looking inside the illuminated cavity. The focus is set on the applicator pipe, while the instantaneous field of view (IFOV) of the radiometer in use may well find the hot spots corresponding to the pipe below the grid. Nevertheless, the radiometer does not accurately measure pipe temperatures due to the slit response function (SRF) effect. Because of the SRF, the object's temperature drops as the distance from the radiometer increases. The latter was set in order to encompass in the IR image the maximum pipe extension compliant with the available slot-window carrying the grid. On the other hand, there is the need of getting as close to the target as possible, in the respect of the minimum focal distance.

A preliminary calibration and a suitable procedure have been then adopted. First, aiming to reduce reflections, the glass-pipe, the grid and the cavity walls have been coated with a high emissivity black paint whose value was measured to be $\epsilon_{\perp} = 0.95$ along the normal (perpendicular line drawn to the surface). In principle, this value is directional and as such it is affected by the relative position of the target with respect to the IR camera.

Then the following two configurations have been considered:

- a) the “test configuration”, i.e. the applicator-pipe carrying the fluid @ fixed inlet temperature.
- b) the “reference configuration”, i.e. a polystyrene slab placed inside the cavity in order to blind the pipe to the camera view. The slab was black painted to realize a normal emissivity of 0.95 and its temperature, T_{slab} , was measured by four fiberoptic probes.

For both (a) and (b) configurations, neglecting the atmosphere contribution, the fundamental equation of IR thermography relates the spectral radiant power incident on the radiometer to the radiance leaving the surface under consideration. For the case at hand, the attenuation due to the grid must be taken into account. The radiance coming from the inner walls is attenuated by a factor τ , which can be defined as “grid transmittance”, which accounts for the SRF grid effect. The latter parameter depends on both the geometry and the temperature level involved. Additionally, the radiometer receives both the radiance reflected from the external surroundings ambient to the grid and the emission by the grid itself. The inner and outer surrounding environments are considered as a blackbodies @ uniform temperatures T_i and T_o , respectively. Finally, the radiometric signal weighted over the sensitivity band by the spectral response of the detection system, including the detector sensitivity, the transmissivity of the optical device and amplification by the electronics, is proportional to the target radiance as follows:

$$I(T_{\text{slab}}^{\text{app}}) = \tau [\epsilon I(T_{\text{slab}}) + (1-\epsilon) I(T_i)] + (1-\tau) [\epsilon I(T_{\text{grid}}) + (1-\epsilon) I(T_o)] \quad (15)$$

$$I(T_{\text{pipe}}^{\text{app}}) = \tau [\epsilon I(T_{\text{pipe}}) + (1-\epsilon) I(T_i)] + (1-\tau) [\epsilon I(T_{\text{grid}}) + (1-\epsilon) I(T_o)] \quad (16)$$

where:

(1) I is the blackbody Planck's function, evaluated at a suitable wavelength, within the radiometer spectral sensitivity window, λ^+ . With reference to the radiometer in use, this latter parameter turns out to be $\lambda^+ = 11.5 \mu\text{m}$ as obtained by instrument calibration data.

(2) the apparent temperatures are the surface ones given by an equivalent blackbody as seen by the IR equipment, both for the pipe, $T_{\text{pipe}}^{\text{app}}$, and the polystyrene slab, $T_{\text{slab}}^{\text{app}}$.

In the above equations, the grid transmittance must be considered strongly dependent on the position since the grid contribution to emission assumes a different weight from point to point. In facts, in spite of the tangential air flow running over the grid, an irregular temperature distribution is still observed, probably arising as an after effect of eddy currents occurrence. The calibration curve related to the specific radiometer allows the retrieval of apparent temperatures, see next paragraph. The exogen contributions due to both the reflections arising from inner and outer walls clearly appear. Only the former contribution is attenuated by the presence of the grid. The last contribution represents the reinforcement due to the grid emission.

Subtracting the two previous equations (15) and (16), the contributions due to both the grid and the inner and outer environments cancel, thus yielding "the net equivalent emissivity for cold surroundings", $\varepsilon\tau$ -function:

$$\varepsilon\tau = \frac{I(T_{\text{pipe}}^{\text{app}}) - I(T_{\text{slab}}^{\text{app}})}{I(T_{\text{pipe}}) - I(T_{\text{slab}})} \quad (17)$$

Most commonly in thermography, the subtraction (Figure 6.4) of images related to configurations (a) and (b) produces the further benefit of cancelling the grid established uneven temperature distribution.

In order to explicit the dependence of I on temperature, the approximations resumed in the sketch (14) were considered; in particular, with reference to the radiometer used during the experiments, $n = 5 \cdot \lambda_{\text{max}}/\lambda^+$. Finally, eq. (17) can be set as:

$$\varepsilon\tau = \frac{(T_{\text{pipe}}^{\text{app}})^{n(T_{\text{pipe}}^{\text{app}})} - (T_{\text{slab}}^{\text{app}})^{n(T_{\text{slab}}^{\text{app}})}}{(T_{\text{pipe}})^{n(T_{\text{pipe}})} - (T_{\text{slab}})^{n(T_{\text{slab}})}} \quad (18)$$

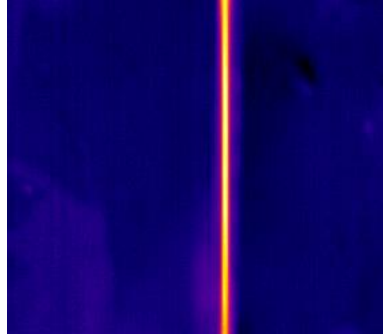


Figure 6.4 Net apparent applicator pipe temperatures

The notation resembles that the index n depends on the temperature itself, through the Wien's law applied to determine λ_{\max} .

In view of this equation, provided the apparent temperatures are known via IR thermography and the slab temperature via the fiberoptic probes, the function $\varepsilon\tau$ is required in order to infer the pipe temperature. The calibration is then intended to determine the $\varepsilon\tau$ as function of both geometry and temperature levels. The calibration is carried on as follows. First, the water flow discharge was kept as high as a linear temperature increase could be experienced for the bulk temperature of the flowing fluid [74]. Thus, measuring the fluid inlet and outlet temperatures by thermocouples placed externally to the illuminated cavity, allowed to know the true bulk water temperature along the longitudinal x axis of the pipe, $T_{\text{pipe}}^{\text{bulk}}(x)$. On the other hand, the need of realizing high flow rates determined temperature increases contained within $\Delta T_{\text{bulk}} = 2.1^\circ\text{C}$ and thus allowed to fix the corresponding temperature level for the test at hand. Seven inlet temperatures, namely $T_{\text{inlet}} = 40, 50, 55, 60, 65, 70$ and 75°C , were considered which covered the temperature range involved in the successive experimental tests.

Assuming that the surface pipe temperature closely approaches the fluid bulk temperature, knowing the apparent temperatures via IR thermography and measuring the slab temperature, eq. (18) allows to evaluate $\varepsilon\tau$ as function of the axial coordinate along the tube longitudinal axis (x) in correspondence of the seven preset true temperature levels, $T = (T_{\text{inlet}} + T_{\text{outlet}})/2$.

In particular, since the relative-shape of the $\varepsilon\tau$ -function along the axial coordinate appeared to be the same but its level was increasing with temperature level (Figure 6.5), the $\varepsilon\tau$ -function was sought as: $\varepsilon\tau(x, T) = f_1(x) + f_2(T)$.

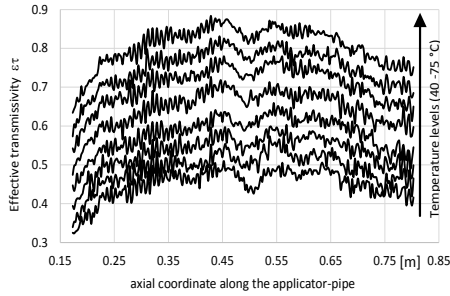


Figure 6.5 Effective transmissivity for the selected temperature levels

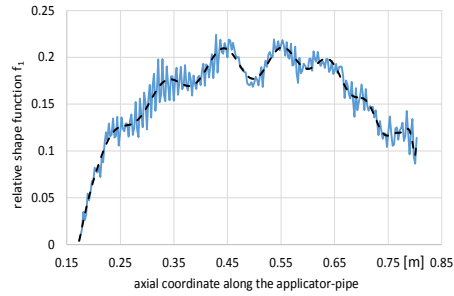


Figure 6.6 Measured and interpolated relative shape-function f_1

The function $f_1(x)$ was recovered by averaging the seven relative shapes and turned out to be well approximated ($R^2 = 0.996$) by a 49-th order polynomial, Figure 6.6, while $f_2(T)$ to be almost linear with temperature, Figure 6.7, the maximum relative error being contained within 3.2%, i.e. $R^2 = 0.996$. As an example, the measured $\varepsilon\tau$ -function @ 55°C is compared with the corresponding one based on the above interpolating structure in Figure 6.8: the satisfying agreement is witnessed by an average relative error contained within 2.3%.

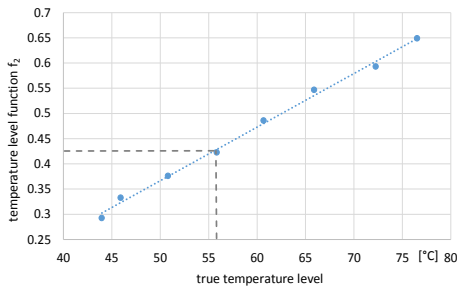


Figure 6.7 Temperature level function f_2 obtained with a linear regression

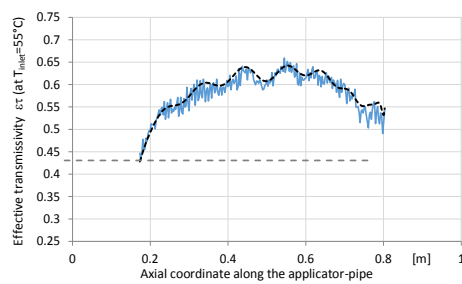


Figure 6.8 The reconstructed and measured true temperature profiles @ $T_{inlet} = 55^\circ\text{C}$

Applying the same procedure to the remaining selected temperature levels similarly shows that measured and reconstructed curves fairly agree, thus showing that the procedure at hand fits well the experimental data. The maximum among the average relative errors corresponding to the selected temperature levels is 3 %.

The knowledge of the $\varepsilon\tau$ -function enables the IR image processing described in the following section.

6.4 Image processing

In view of the discussion previously presented, tests related to configuration (a) were performed. Provided steady conditions were attained, an image sequence at the rate of 10 images per second was taken for two seconds. Since frames in time sequence differ only in the distribution of random noise, twenty frames were averaged to form a single image with noise variance reduced proportionally to the sequence length. Performing a horizontal scan of the formed image, the maximum apparent temperature for each row was extracted, identifying in such way the proper pipe longitudinal apparent temperature.

In a similar fashion, processing an image sequence related to configuration (b), the apparent slab temperatures were extracted in correspondence of the pixels selected by processing configuration (a). Finally, eq. (18) was solved for each point x along the pipe axis in terms of the unknown true pipe temperature T_{pipe} , T_{slab} being measured by the fiberoptic probes.

6.5 Results and discussion

Applying the procedure described in the previous paragraphs, the experimental tests were performed considering three temperature levels, namely 40 °C, 45 °C and 50 °C and two flow rates, that is 3.2 and 5.5 g/s. Data reduction showed that the level of the resulting temperature profile is very sensitive to the slab true temperature, known only in few points. Moreover, the fiberoptic probes, placed at different heights of the slab, proved that the latter is featured by an almost uniform temperature, the variations of the values measured being contained in 2.5 °C. The variations of this parameter have been related to a criterion, following the indications of the numerical results. In particular, the enhanced hybrid solution was obtained according to the procedure described in the chapter

5. Thermal and dielectric properties used during the numerical simulations were evaluated in correspondence of the average temperature of the flowing liquid resulting from the experiments. After processing the numerical results, the level of the experimental temperature profiles was adapted modifying the slab temperature such that the experimental average temperature recovered the numerical one, evaluated in the “window” observed. Furthermore, it was verified that the variations of the slab temperature needed were contained in the range of $\pm 2^\circ\text{C}$ and a temperature level consistent with the thermocouples placed at the inlet and outlet sections was recovered.

A further criterion could be the introduction of a fiberoptic probe inside the pipe, with the aim of measuring the water bulk temperature at a fixed height in the “window” observed. Thus, in this case, the latter parameter is the reference value to be recovered, by modifying the slab temperature. Following the first criterion, the experimental temperature profiles were processed and were compared with the numerical ones, as shown in Figure 6.9. In particular, the attention was put on the shapes of the theoretical curves, which resemble the experimental ones. A quite satisfying agreement exists, at least in terms of qualitative behaviour: the uneven temperature distribution which is due, in turn, to the EM field patterns, seems to be recovered.

The corresponding RMSE values, as shown in Table 6.1, confirm that increasing the flow rates increases the accuracy of the prediction. This occurrence is expected since the uneven temperature distribution inside pipe section is reduced with increasing the fluid average speed [74]; thus, the bulk temperature values are closely approached by the wall temperature in each section in correspondence of higher flow rates, as supposed in advance.

Mass flow rate [g/s]	Tinlet [$^\circ\text{C}$]	RMSE [$^\circ\text{C}$]
3.2	40	1.7
3.2	45	1.8
3.2	50	1.7
5.4	40	1.3
5.4	45	1.4
5.4	50	1.1

Table 6.1 RMSE of bulk temperatures for different mass flow rates and temperature levels

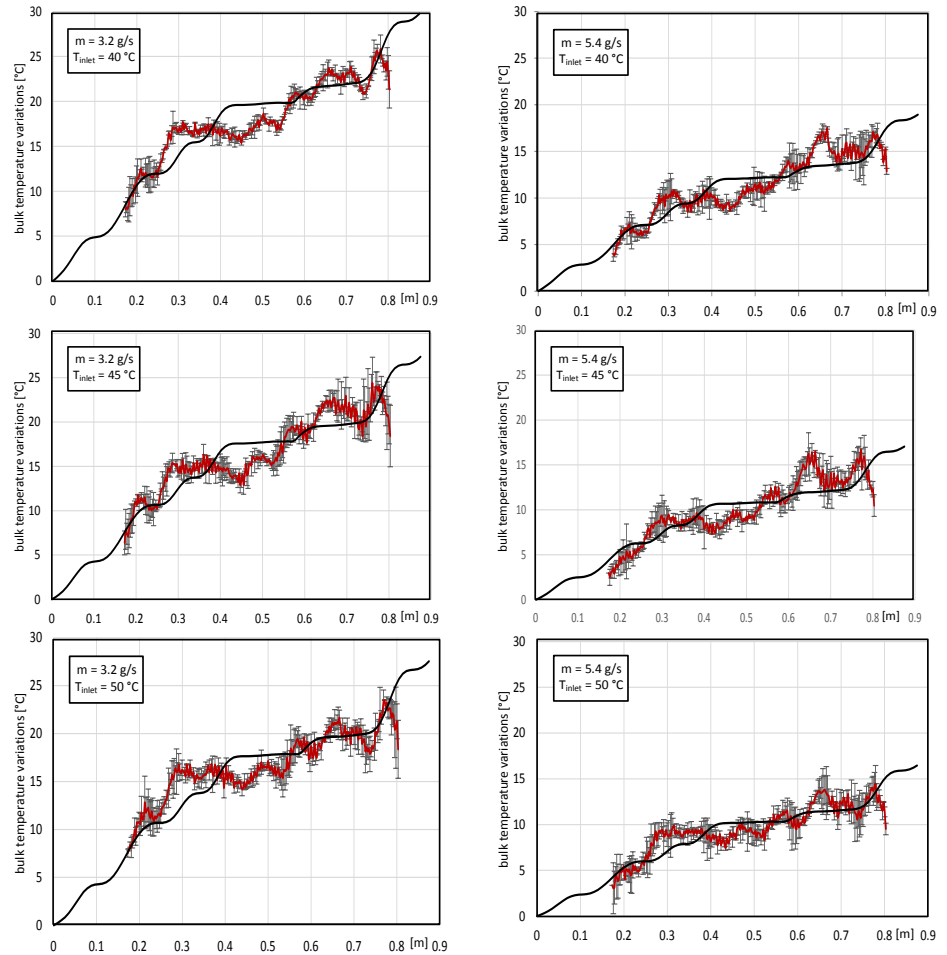


Figure 6.9 Theoretical and experimental bulk temperatures for inlet temperatures $T_{\text{inlet}} = 40, 45$ and $50 \text{ }^\circ\text{C}$, and two flow rates $m = 3.2$ and 5.4 g/s .

CONCLUSIONS

The purpose of this thesis is the analysis of microwave heating processes, offering a contribution for temperature distribution measurement and control as well as for the numerical-analytical prediction. In particular, after a brief description of the principles of microwave heating, some batch processes have been analysed, that is, apple drying and in-package heating of water and oil. In both cases, the use of infrared technique allowed to obtain the spatial temperature distribution of the samples under test.

Microwave drying has been applied to apple slices, and IR temperature detection allowed to keep under control their surface average thermal level in time; thus, this enables to follow the temperature-time curves during MW heating, according to the process at hand, within the limits specified.

An isothermal 2D unsteady model for mass transfer was employed to describe the measured drying kinetics of apples. Quite satisfying results were obtained applying the model to recover experimental data, probably due to operating at fixed temperature levels for the samples under test.

The analysis of the second kind of batch tests considered, the in-package heating of water and oil, allowed to show the sensitivity of the temperature distribution to the orientation of the samples, the mass and the dielectric properties. Moreover, a finite element method software, Comsol Multiphysics, was used to develop a 3D numerical model, in order to predict the temperature distribution of the samples surface. By comparing experimental and numerical results, it was proven that the proposed finite-element simulation strategy is quite robust and can be suitably extended to encompass more complicated and realistic problems involving MW heating.

In the second section of the thesis, the continuous flow microwave heating processes have been analysed. The main aim was to develop a theoretical instrument, able to predict the bulk temperature distribution without great computational efforts. It was demonstrated that, in absence of significant temperature variations and for high velocities, constant dielectric properties can be considered, and an analytical model, accounting for uniform heat generation inside the liquid, could be used. Thus, it has been proven that, under suitable conditions, a quick response

can be obtained adopting the analytical model. In the other cases, it's necessary to take into account the modifications of the dielectric properties during the process; at this aim, an hybrid numerical-analytical solution was developed, which was compared with the one obtained by Comsol Multiphysics, considering the temperature dependence of the dielectric permittivity; the complete numerical solution (CN), because of the coupling of the heat transfer problem and the electromagnetic problem, required a great computational time. Unlike this, the new hybrid numerical solution reduced the time required for computation, obtaining only the electromagnetic solution with the numerical instrument and considering constant dielectric properties. The temperature dependence of the dielectric permittivity was included through a manipulation of the heat generation distribution, introducing a weighting function opportunely chosen: the latter took into account the variations of the dielectric loss factor. Thus, the heat transfer problem was analytically solved, feeding the heat generation term with the one obtained interpolating the weighted discrete heat generation distribution, using the Fourier Discrete Transform. The solution found by the described procedure was named "Enhanced Hybrid" (EH), because it improves the so-called "Basic Hybrid solution" (BH) through the introduction of the weighting function. Finally, a theoretical-experimental procedure was developed to measure the bulk temperature distribution in water flowing in a glass-pipe, subjected to microwaves. High-resolution thermal maps in real time were obtained by processing infrared thermographic images. Considering the equation of thermography for the case at hand, the temperature distribution with high resolution was obtained after a suitable calibration; the latter was required because of the presence of the grid. Thus, the developed procedure offers a great contribution for temperature measurement inside the microwave oven, taking into account that usually temperature is measured in few points. Such an approach is needed, since the uneven EM field causes an uneven spatial distribution of the temperature field.

In order to check the goodness of the fast hybrid model previously developed, the experimental results were compared with the EH solution, showing an acceptable agreement, with a better prediction for higher flow rates.

References

- [1] T.D. Durance and J.H. Wang; "Energy Consumption, Density, and Rehydration Rate of Vacuum Microwave- and Hot-Convection-Dehydrated Tomatoes", *Journal of Food Science*, Vol. 67, Nr. 6, 2002
- [2] Jasim Ahmed and Hosahalli S. Ramaswamy, "Microwave Pasteurization and Sterilization of Foods", *Handbook of Food Preservation*, Second Edition, Chapter 28.
- [3] M. Maskan and F. Gogus, "Sorption isotherms and drying characteristics of mulberry (*Morus alba*)", *J. Food Eng.*, 37 (1998).
- [4] N. R. Pereira, A. Marsaioli Jr., L. M. Ahrne, Effect of microwave power, air velocity and temperature on the final drying of osmotically dehydrated bananas, *Journal of Food Engineering*, 81 (2007)
- [5] Alibas, "Microwave, air and combined microwave – air drying parameters of pumpkin slices", *LWT*, 40 (2007)
- [6] G. Dadali, D. Kılıç Apar and B. Özbek, "Microwave drying kinetics of okra", *Dry. Tech.* 25 (2007)
- [7] J. Wang and K. Sheng, "Far Infrared and microwave drying of peach", *LWT Food Science and Technology*, 39 (2006).
- [8] Z. Wang, J. Sun, F. Chen, X. Liao and X. Hu, "Mathematical modeling on thin layer microwave drying of apple pomace with and without hot air pre-drying", *Journal of Food Engineering*, 80 (2007).
- [9] B. Ozbek and G. Dadali, "Thin layer drying characteristics and modeling of mint leaves undergoing microwave treatment", *Journal of Food Engineering*, 83 (2007)
- [10] Alibas, "Characteristics of chard leaves during microwave, convective, and combined microwave – convective drying", *Drying Technology*, 24 (2006)
- [11] Prabhanjan, D. G., Ramaswamy, H. S. & Raghavan, G. S. V., "Microwave-assisted convective air drying of thin layer carrots", *Journal of Food Engineering*, 25 (2) (1995).
- [12] B. Al-Duri and S. McIntyre, Comparison of drying kinetics of food using a fan- assisted convection oven, a microwave oven and a combined microwave/convection oven, *J. Food Eng.*, 15 (1992)
- [13] J. Wang and Y. S. Xi, "Drying characteristics and drying quality of carrot using a two stage microwave process", *J. Food Eng.*, 68 (2005)

- [14] J. Wang, J. S. Wang and Y. Yu, "Microwave drying characteristics and dried quality of pumpkin", *International Journal of food science and Technology*, 42 (2007).
- [15] Zhenfeng Li, G.S.V. Raghavan, Valérie Orsat, "Temperature and power control in microwave drying", *Journal of Food Engineering*, 97 (2010)
- [16] Adedeji, A.A., Ngadi, M.O., Raghavan, G.S.V., "Kinetics of mass transfer in microwave precooked and deep-fat fried chicken nuggets", *Journal of Food Engineering*, 91 (1) (2009)
- [17] Changrue, V., Orsat, V., Raghavan, G.S.V., "Osmotically dehydrated microwave-vacuum drying of strawberries", *Journal of Food Processing and Preservation*, 32 (5) (2008)
- [18] Sumnu, G., Turabi, E., Oztop, M., "Drying of carrots in microwave and halogen lamp-microwave combination ovens", *Lebensmittel Wissenschaft und Technologie* 38, 549–553, 2005
- [19] Contreras, C., Martín-Esparza, M.E., Chiralt, A., Martínez-Navarrete, N., "Influence of microwave application on convective drying: effects on drying kinetics, and optical and mechanical properties of apple and strawberry", *Journal of Food Engineering* 88, 55–64, 2008
- [20] Andres, A., Bilbao, C., Fito, P., "Drying kinetics of apple cylinders under combined hot air-microwave dehydration", *Journal of Food Engineering* 63, 71–78, 2004
- [21] Bilbao-Sáinz, C., Andrés, A., Chiralt, A., Fito, P., "Microwaves phenomena during drying of apple cylinders", *Journal of Food Engineering* 74, 160–167, 2006
- [22] M. Al-Harashseh, A. H. Al-Muhtaseb, and T. R. A. Magee, "Microwave drying kinetics of tomato pomace: Effect of osmotic dehydration", *Chem. Eng. Process*, 48 (2009).
- [23] G. Dadali and B. Ozbek, "Microwave heat treatment of leek: drying kinetic and effective moisture diffusivity", *International Journal of Food Science and Technology*, 43 (2008)
- [24] G. P. Sharma and S. Prasad, "Effective moisture content of garlic cloves undergoing microwave – convective drying", *Journal of Food Engineering*, 65 (2004).
- [25] H. Torgul, "Suitable drying model for infrared drying of carrot", *Journal of Food Engineering*, 77 (2006)

- [26] Cheremisinoff, N. P., "Fundamentals of Momentum and Heat Transfer, Handbook of Heat and Mass Transfer", Houston, Texas: Gulf, (1986)
- [27] Demirel, D., & Turhan, M., "Air-drying behaviour of Dwarf Cavendish and Gros Michel banana slices", *Journal of Food Engineering*, 59 (1) (2003)
- [28] Iguaz, A., San Martín, M. B., Maté, J. I., Fernández, T., & Vírveda, "Modelling effective moisture diffusivity of rough rice (Lido cultivar) at low drying temperatures", *Journal of Food Engineering*, 59 (2-3) (2003)
- [29] Salvatori, D., Andrés, A., Chiralt, A., & Fito, P., "Osmotic dehydration progression in apple tissue. I: Spatial distribution of solutes and moisture content", *Journal of Food Engineering*, 42 (1999)
- [30] Cui, Z. -W., Xu, S. -Y., & Sun, D. -W., "Microwave-vacuum drying kinetics of carrot slices", *Journal of Food Engineering*, 65 (2) (2004).
- [31] G. Cuccurullo, P. G. Berardi, "Elementi di termodinamica e trasmissione del calore", chapter 5
- [32] Incropera, DeWitt, Bergman, Lavine, "Fundamentals of heat and mass transfer", chapter 14
- [33] J.I. Lombraña, R. Rodríguez, U. Ruiz, "Microwave-drying of sliced mushroom. Analysis of temperature control and pressure", *Innovative Food Science and Emerging Technologies*, 11 (2010).
- [34] Duygu Evin, "Microwave drying and moisture diffusivity of white mulberry: experimental and mathematical modeling", *Journal of Mechanical Science and Technology*, 25 (10) (2011)
- [35] D. Velić, M. Planinić, S.Tomas, M. Bilić, "Influence of airflow velocity on kinetics of convection apple drying", *Journal of Food Engineering*, 64 (2004)
- [36] Alzamora, S., Thesis, Facultad de Ciencias Exactas y Naturales, Universidad de Buenos Aires, Argentina, 1979
- [37] Labuza, T.P. and Simon, I.B., "Air drying of apples slices", *Food Technology*, 24 (1970)
- [38] Rostein, E., Laura, P., A. and Cemborain, M.E., "Analytical prediction of drying performances in non-conventional shapes", *Journal of Food Science*, 39 (1974).
- [39] Cui, Z.W., Xu, S.Y., Sun, D.W., Chen, W., "Temperature changes during microwave-vacuum drying of sliced carrots", *Drying Technology*, 23 (2005)

- [40] Clary, C.D., Wang, S., Petrucci, V.E., "Fixed and incremental levels of microwave power application on drying grapes under vacuum", *Journal of Food Science*, 70 (5) (2005)
- [41] Lu, L., Tang, J., Ran, X., "Temperature and moisture changes during microwave drying of sliced food", *Drying Technology*, 17 (1999)
- [42] Zhang, M., Tang, J., Mujumdar, A.S., Wang, S., "Trends in microwave-related drying of fruits and vegetables, *Trends in Food & Technology*", 17 (2006),
- [43] Drouzas, A. E., & Schubert, H. "Microwave application in vacuum drying of fruits", *Journal of Food Engineering*, 28 (3) (1996).
- [44] Erle, U., & Shubert, H. "Combined osmotic and microwave-vacuum dehydration of apples and strawberries", *Journal of Food Engineering*, 49 (2) (2001).
- [45] Li, Z., Raghavan, G.S.V., Wang, N., "Carrot volatiles monitoring and control in microwave drying", *LWT–Food Science and Technology* (2009a)
- [46] Zhenfeng Li, G.S. V. Raghavan, Ning Wang, Yvan Gariépy, "Real-time, volatile-detection-assisted control for microwave drying", *Computers and Electronics in Agriculture*, 69 (2009)
- [47] Gordon L., Robertson, *Food Packaging: Principles and Practice*, Vadivambal CRC Press, 2012
- [48] R. Vadivambal, D. S. Jayas, "Non-uniform temperature distribution during microwave Heating of Food Materials - A Review", *Food Bioprocess Technol*, vol. 3, pp.161–171, (2010)
- [49] T.Santos, L.C. Costa, M.Valente, J.Monteiro, J.Sousa, "3 D Electromagnetic Field Simulation in Microwave Ovens: a Tool to Control Thermal Runway", Excerpt from the Proceedings of the Comsol Conference 2010 Paris
- [50] H.W. Yang, S. Gunasekaran, "Comparison of temperature distribution in model food cylinders based on Maxwell's equations and Lambert's law during pulsed microwave heating", *Journal of Food Engineering* 64, 445–453, (2004)
- [51] G. Cuccurullo, L. Giordano, D. Albanese, L. Cinquanta, M. Di Matteo, "Infrared thermography assisted control for apples microwave drying", *Journal of food engineering*, vol. 112; p. 319-325, (2012)
- [52] W. Cha-um, P. Rattanadecho, W. Pakdee, "Experimental and Numerical Analysis of Microwave Heating of Water and Oil Using a

- Rectangular Wave Guide: Influence of Sample Sizes, Positions, and Microwave Power”, *Food Bioprocess Technol*, 4:544–558, (2011)
- [53] Hamid, M.A.K., Boulanger, R.J., Tong, S.C., Gallop, R.A. and Pereira, R.R., Microwave pasteurization of raw milk. *J. Microwave Power*, 4, 272–275, 1969.
- [54] LeBail, A., Koutchma, T. and Ramaswamy, H.S., Modeling of temperature profiles under continuous tube-flow microwave and steam heating conditions. *Food Process Eng.* 23, 1–24, 1999.
- [55] Koutchma, T., LeBail, A. and Ramaswamy, H.S., Modeling of process lethality in continuous-flow microwave heating-cooling system, in *Proc. Int. Microwave Power Institute, Chicago*, 74–77, 1998.
- system for apple cider. *Lebensm.-Wiss. u.-Technol.* 38, 227–238, 2005.
- [56] Tajchakavit, S. and Ramaswamy, H., Continuous-flow microwave heating of orange juice: Evidence of non-thermal effects. *J. Microwave Power Electromag. Energy* 30, 141–148, 1995
- [57] Gentry, T.S. and Roberts, J.S., Design and evaluation of a continuous flow microwave pasteurization system for apple cider. *Lebensm.-Wiss. u.-Technol.* 38, 227–238, 2005
- [58] Tanmay Basak, “Role of Various Elliptical Shapes for Efficient Microwave Processing of Materials”, *AIChE Journal*, Vol. 53, No. 6, pp. 1399 – 1412, (2007)
- [59] Caponio F., Pasqualone A., Gomes T., “Effects of conventional and microwave heating on the degradation of olive oil”, *European Food Research Technology*, 215:114-117, (2002)
- [60] Development of packaging and products for use in microwave oven, edited by Matthew W. Lorence and Peter S. Pesheck
- [61] COMSOL Multiphysics Version 4.3a User guide, Released October 1st, 2012.
- [62] O.C. Zienkiewicz, R.L. Taylor, J.Z. Zhu, 2005. *The Finite Element Method: Its Basis and Fundamentals* (Sixth ed.). Butterworth-Heinemann. ISBN 0750663200
- [63] Prapuchanay, E., Puangngernmak N., Chalermwisutkul S., “A single mode cylindrical microwave cavity for heating applications of liquid material”, 9th International Conference on Electrical Engineering/Electronics, Computer, Telecommunications and Information Technology (ECTI-CON), pp. 1-4, 2012

- [64] Pranjali D. Muley, Dorin Boldor, “Multiphysics Numerical Modeling of the Continuous Flow Microwave-Assisted Transesterification Process”, *Journal of Microwave Power and Electromagnetic Energy*, vol. 46, no. 3, pp. 139-162, 2012
- [65] D. Salvi, J. Ortego, C. Arauz, C.M. Sabliov, D. Boldor, “Experimental study of the effect of dielectric and physical properties on temperature distribution in fluids during continuous flow microwave heating”, *Journal of Food Engineering* vol. 93, pp. 149–157, 2009
- [66] D. Salvi, D. Boldor, G.M. Aita, C.M. Sabliov, “COMSOL Multiphysics model for continuous flow microwave heating of liquids”, *Journal of Food Engineering*, vol. 104, pp. 422–429, 2011
- [67] J.Zhu, A.V. Kuznetsov, K.P. Sandeep, “Mathematical modeling of continuous flow microwave heating of liquids (effects of dielectric properties and design parameters)”, *International Journal of Thermal Sciences*, vol. 46, pp.328-341, 2007
- [68] Q. Zhang, T.H. Jackson, A. Ungan, “Numerical modeling of microwave induced natural convection”, *International Journal of Heat and Mass Transfer*, vol. 43, pp. 2141–2154, 2000
- [69] D. Salvi, Dorin Boldor, J. Ortego, G. M. Aita, C. M. Sabliov, “Numerical Modeling of Continuous Flow Microwave Heating: A Critical Comparison of Comosl and Ansys”, *Journal of Microwave Power and Electromagnetic Energy*, vol. 44, no. 4, pp. 187-197, 2010
- [70] D. Salvi, J. Ortego, C. Arauz, C.M. Sabliov, D. Boldor, “Experimental study of the effect of dielectric and physical properties on temperature distribution in fluids during continuous flow microwave heating”, *Journal of Food Engineering* vol. 93, pp. 149–157, 2009
- [71] C. Mirabito, A. Narayanan, D. Perez, B. Stone, FEMLAB model of a coupled electromagnetic–thermal boundary value problem. Research Experience: Worcester Polytechnic Institute, MA, 2005
- [72] A. Datta, H. Prosetya, and W. Hu, “Mathematical modeling of batch heating of liquids in a microwave cavity,” *Journal of Microwave Power and Electromagnetic Energy*, 1992, vol. 27, no. 1, pp. 38–48.
- [73] G. Cuccurullo, L. Giordano, G. Viccione, 2014, A fast and accurate hybrid model for simulating continuous pipe flow microwave heating of liquids, *International Journal of Mechanics*, 8(1), pp. 45–52.
- [74] G. Cuccurullo, L. Giordano, G. Viccione, 2013, An analytical approximation for continuous flow microwave heating of liquids, *Advances in Mechanical Engineering*.

- [75] P. Ratanadecho, K. Aoki, and M. Akahori, "A numerical and experimental investigation of the modeling of microwave heating for liquid layers using a rectangular wave guide (effects of natural convection and dielectric properties)," *Applied Mathematical Modelling*, 2002, vol. 26, no. 3, pp. 449–472.
- [76] D. A. Salvi, D. Boldor, C.M. Sabliov, and K. A. Rusch, "Numerical and experimental analysis of continuous microwave heating of ballast water as preventive treatment for introduction of invasive species," *Journal of Marine Environmental Engineering*, 2008, vol. 9, no. 1, pp. 45–64.
- [77] K.S. Yee, "Numerical solution of initial boundary value problem involving Maxwell's equations in isotropic media," *IEEE Transactions on Antennas and Propagation*, 1966, vol. 14, pp. 302-307.
- [78] S. Chatterjee, T. Basak, and S.K. Das, "Microwave driven convection in a rotating cylindrical cavity: a numerical study", *Journal of Food Engineering*, 2007, vol. 79, pp. 1269-1279.
- [79] J. Zhu, A. V. Kuznetsov, and K. P. Sandeep, "Investigation of a particulate flow containing spherical particles subjected to microwave heating," *Heat and Mass Transfer*, 2008, vol. 44, no. 4, pp. 481–493.
- [80] V.V. Yakovlev, "Examination of contemporary electromagnetic software capable of modeling problems of microwave heating", in: M. Willert- Porada (Ed.), *Advances in Microwave and Radio Frequency Processing*, Springer Verlag, 2005, pp. 178-190.
- [81] A. Mamouni, J.C. Van De Velde, Y. Leroy, 1981, New correlation radiometer for microwave thermography, *ibid.*, 1981, 17, pp. 554-555.
- [82] A. Mamouni, Y. Leroy, J.C. Van De Velde, L. Bellarbi, 1983, Introduction to correlation microwave thermography, *J. Microwave Power*, 18, pp. 285–293.
- [83] S.K. Jacobsen, Ø. Klemetsen, Y. Birkelund, 2012, Vesicoureteral reflux in young children: a study of radiometric thermometry as detection modality using an ex vivo porcine model, *Physics in Medicine and Biology*, 57(17), pp. 5557 – 5573.
- [84] N.M. Gerbo, D. Boldor, C.M. Sabliov, "Design of a measurement system temperature distribution in continuous-flow microwave heating of pumpable fluids using infrared imaging and fiber", *Optic Technology*, vol. 42, no. 1, pp. 55–65, 2008
- [85] Cuccurullo G., Giordano L., Viccione G., Quantitative IR Thermography for Continuous Flow Microwave Heating, *WSEAS*

Transactions on Heat and Mass Transfer 01/2014; E-ISSN: 2224-3461(9):234.

[86] G.Cuccurullo, L.Giordano, L.Cinquanta, M.Migliozzi, "Heating uniformity investigation in microwave batch processing of water and oil", Procs. of the 18th International Conference on Thermal Engineering and Thermogrammetry (THERMO), Budapest, 3-5 Luglio 2013, mate, ISBN: 9789638231970

[87] Cuccurullo G., Giordano L., Albanese D.; "IR thermography assisted control for apples microwave drying", Procs. of the QIRT 2012 - 11th Quantitative InfraRed Thermography ,Napoli, 11-14 giugno 2012, edito da Gennaro Cardone, ISBN: 9788890648441,(2012)

[88] User's manual, ThermaCAM P65, FLIR SYSTEMS, 2006